MONTHLY AND SEASONAL SIMULATIONS WITH THE GLAS CLIMATE MODEL

David A. Randall

NASA/Goddard Space Flight Center

Goddard Laboratory for Atmospheric Sciences

Greenbelt, MD 20771 U.S.A.

1. INTRODUCTION

The GLAS climate model is being used in studies of the predictability of monthly and seasonal means, and in tests of the sensitivity of the general circulation to boundary forcings such as anomalies of sea surface temperature or soil moisture.

In this paper, we present results obtained with two versions of the model. The 1980 model has been described and its ability to simulate winter and summer monthly means has been extensively analyzed in a report by Shukla et al. (1982). Sections 2 and 3 of the present paper are a condensed version of that report. The 1982 model is described by Randall et al. (1982c), and a brief description is given in Section 4 of the present paper. The newer model has been used in a 400-day simulation of the seasonal cycle. Some preliminary results from this long run are given in Section 5.

2. 1980 MODEL DESCRIPTION AND BOUNDARY CONDITIONS

The 1980 version of the GLAS climate model evolved from the GISS GCM, described by Sommerville et al. (1974) and Stone et al. (1977), which in turn, was based on the 3-level 1970 version of the GCM developed by A. Arakawa (1972) and Y. Mintz at UCLA. The model used a form of the σ coordinate system (Phillips, 1957), with nine layers, all of the same σ thickness, and a 4 x 5 degree latitude-longitude grid, modified in the polar regions as discussed below. The variables were staggered in the horizontal according to the B-grid scheme of Arakawa and Lamb (1977), and in the vertical according to the scheme of Lorenz (1960). The upper boundary of the model was at 10 mb. The prognostic atmospheric

variables were the surface pressure, the zonal and meridional components of the horizontal wind, the temperature, and the water vapor mixing ratio. The prognostic boundary variables were the bulk ground temperature and ground wetness, and the snow depth.

Although the model was similar to the GISS GCM presented by Somerville et al. (1974) and Stone et al. (1977), significant changes were made in both the finite-difference schemes and the physical parameterizations. As described by Halem and Russell (1973), Halem et al. (1979), and Herman and Johnson (1978), the model incorporated a "split grid," in which the number of grid points on a latitude circle was systematically reduced near the poles. This was intended to improve running speed by allowing the use of a ten-minute time step, with only weak longitudinal smoothing at high latitudes.

Once every simulated half hour, a sixteenth-order Shapiro filter (Shapiro, 1970) was applied, in the longitudinal direction, to the sea level pressure, and to the potential temperature and the wind components on the σ surfaces. The filter was introduced as an ad hoc device to suppress the "checkerboard" noise in the prognostic fields, which arises from the inability of the B-grid to simulate the geostrophic adjustment process at the two grid interval level (Arakawa and Lamb, 1977). However, a substantial price was paid for this noise suppression. Filtering the potential temperature on the σ surfaces leads to a systematic cooling of the air over mountains and a systematic warming in the neighboring valleys. Filtering of the winds dissipates kinetic energy. Filtering of the sea-level pressure interferes with every conservation property of the model (except mass conservation). The magnitudes of some of these false, filter-induced sources and sinks were determined. The filtering of potential temperature generates 2.5 W m^{-2} of potential energy, and filtering of the winds dissipates 1.5 W m^{-2} of kinetic energy.

The Matsuno forward-backward time differencing scheme was used. This scheme tends to damp high frequencies, and so it helps to control computational noise

in the model, but at the cost of almost doubling the computing time required for the dynamics. Less storage is needed than with the leapfrog scheme.

The cumulus parameterization is that developed by Arakawa (1969; see also Haltiner, 1971) for the three-level UCLA GCM; but as modified for use in a nine-level GCM by Sommerville et al. (1974; see also Helfand, 1979). The model also included latent heat release due to large-scale saturation, which occurs when the relative humidity exceeds 100%.

The short-wave radiation parameterization is that presented by Lacis and Hansen (1974), as revised and documented by Davies (1982). It includes absorption by ozone, water vapor, and clouds. The long-wave radiation parameterization was based on the method described by Wu (1976), Wu et al. (1978), and Wu (1980) and documented by Krishnamurthy (1982). In order to save computing time, the time step for the long-wave radiation was 5 hours for the simulations presented in this paper.

Clouds were assumed to occur if and only if the model predicts cumulus convection (restricted to the lowest six layers) or large-scale saturation (in any layer). No parameterization of subgrid-scale fractional cloudiness was attempted; both supersaturation and convective clouds were assumed to completely fill a grid box.

The planetary boundary layer (PBL) parameterization was formulated by Katayama, as reported by Arakawa, (1972) and modified by Sommerville et al. (1974) and Sud and Abeles, (1981).

The model incorporated a prognostic soil moisture, following the UCLA model (Arakawa, 1972), but with different formulations for the runoff, snow melt, and potential evapotranspiration, as developed by Lin et al. (1978).

The model used the externally imposed boundary conditions listed in Table 2.1. The topography was smoothed, and in addition the land-surface heights for Greenland were substantially reduced. The observed climatological values of the seasonally varying boundary conditions were archived in the form of monthly

means. A continuously changing set of prescribed sea surface temperatures, surface albedoes, and snow-ice distributions was obtained by assigning the observed monthly-mean values to the midpoint of the appropriate month, and computing the values on all other days by linear interpolation. A further description of the boundary condition data sets is given by Randall et al. (1982a).

Table 2.1

Prescribed Boundary Condition	Data Source	GLAS Data Set Name
Topography	NASA/Goddard Institute for Space Studies	C1APF79T
Sea Surface Temperatures	NOAA/Geophysical Fluid Dynamics Laboratory	C1APF79T
Surface Albedoes	Posey and Clapp (1964)	C1APF79A
Snow/Ice Distributions	British Met. Office (1977) Matson (1977) Robock (1980)	C1APF79S

3. MONTHLY SIMULATIONS

3.1 Initial conditions

The winter simulation described in this section started with the observed state of the atmosphere for 00Z on January 1, 1975. The summer simulation was started with the observed state of the atmosphere for 00Z on June 15, 1979. In both runs, the initial ground temperatures for land and sea ice points were assumed to be equal to the suface air temperature. The initial soil moistures were obtained from climatological surface air relative humidities, as explained by Stone et al. (1977). The initial snow boundaries were obtained from the

climatological data of Matson (1977), and the initial snow depths were specified as functions of the surface albedo.

3.2 Mean prognostic fields

The analysis presented in this subsection was performed by J. Shukla, of GLAS.

Figures 3.1a and 3.2a show the 16-year mean sea level pressure for January and July, reproduced from Godbole and Shukla (1981), and Figures 3.1b and 3.2b show the simulated mean sea level pressure for the single February and July, respectively.

For February, the simulations of the prominent Northern Hemispheric circulation features, such as the Aleutian low, the Icelandic low and the Siberian high are fairly realistic. The discrepancy in the structure and intensity of the Siberian high is too large to be accounted for by the interannual variability or by differences between January and February. The most serious deficiencies of the simulated sea level pressure field in February are in the Southern Hemisphere. The observed sea level pressure is zonally uniform between about 40°S-60°S, while the simulated pressure field is cellular in this zone.

For July, the simulated sea level pressure field is also in fairly good agreement with the observations. The high pressure cell over the North Atlantic is very well simulated both with regard to intensity and to structure. Over the north Pacific the simulated high pressure cell is too small in the east-west direction, and its major axis is oriented NNW-SSE instead of WSW-ENE. The Asiatic monsoon low is well simulated. The subtropical high pressure cells in the Southern Hemisphere are well simulated over the Indian Ocean, Atlantic Ocean and the eastern Pacific but not over Australia. The westerly zonal geostrophic flow that is shown by the isobars between 40°S and 60°S is fairly well simulated over the south Atlantic and south Indian Oceans; but in the south Pacific Ocean the simulated geostrophic flow is easterly between 40°S-60°S. Again, the simulation produces non-zonal isobars in the southern hemispheric mid-latitudes. Figures 3.3a and 3.4a show the observed (Crutcher and Davis, 1969) 200 mb

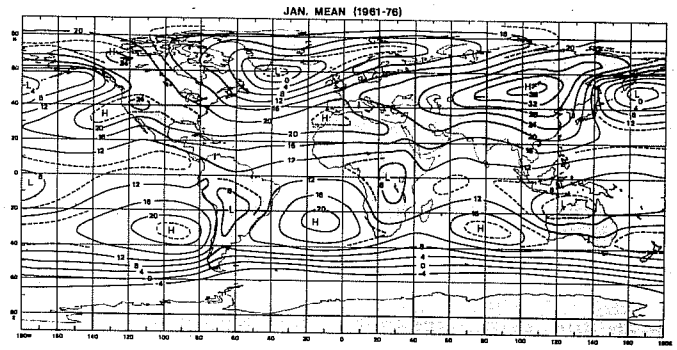

Figure 3.1a Observed mean sea level pressure (-1000 mb) for January (Godbole and Shukla, 1980).

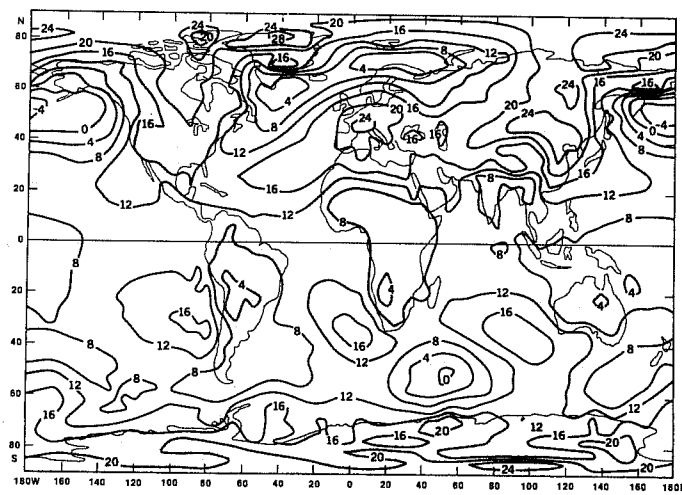

Figure 3.1b Simulated sea level pressure (-1000 mb) for February.

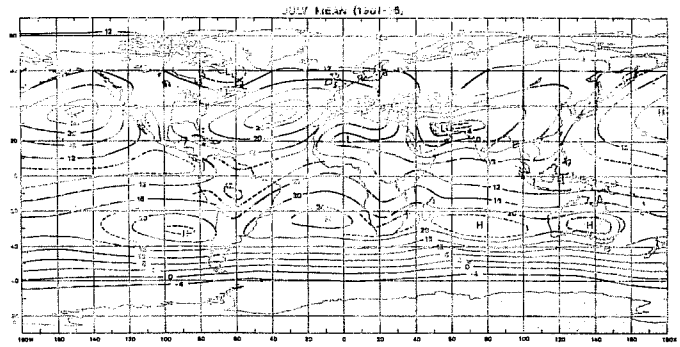

Figure 3.2a Observed mean sea level pressure (-1000 mb) for July (Godbole and Shukla, 1980).

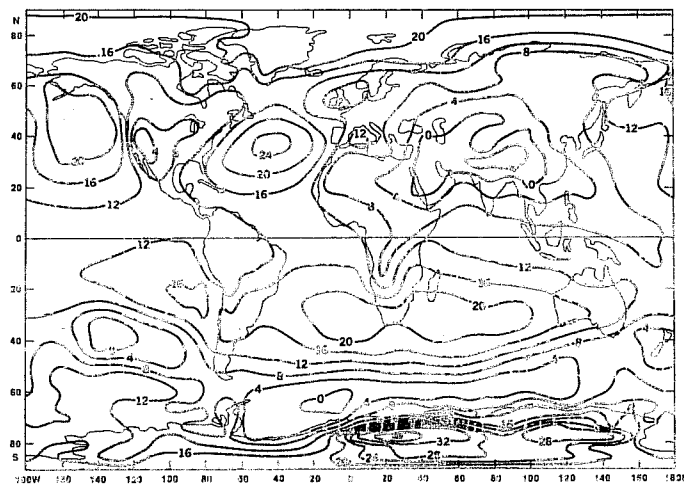

Figure 3.2b Simulated sea level pressure (-1000 mb) for July.

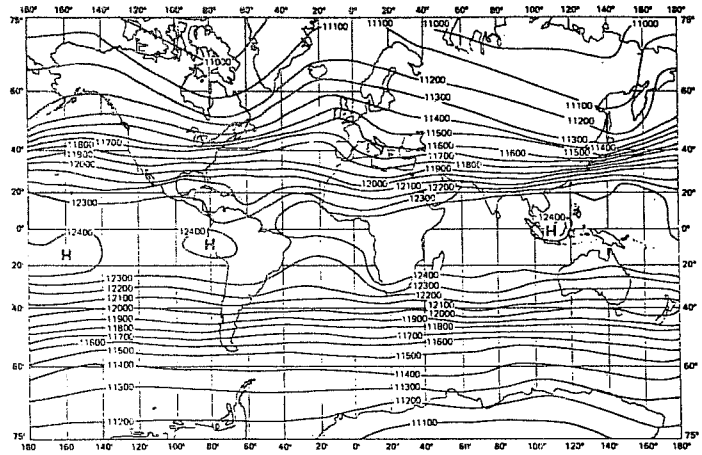

Figure 3.3a Observed mean geopotential height (gpm) at 200 mb for December, January and February (Crutcher and Davis, 1969).

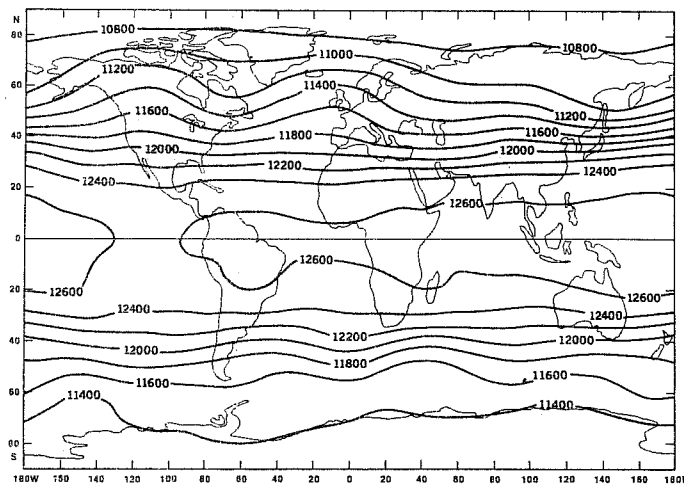

Figure 3.3b Simulated geopotential height (gpm) at 200 mb for February.

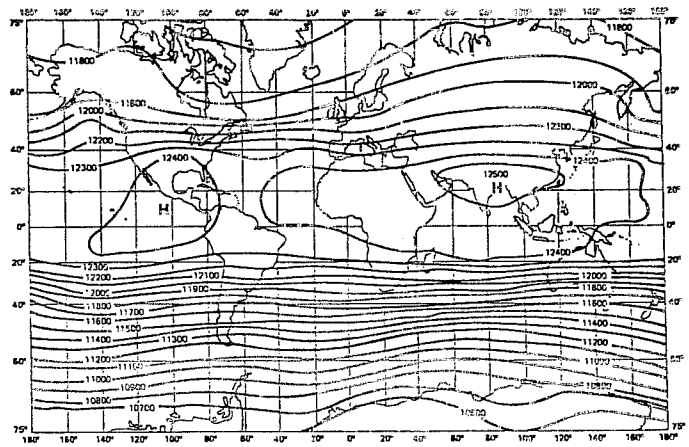

Figure 3.4a Observed mean geopotential height (gpm) at 200 mb for June, July and August (Crutcher and Davis, 1969).

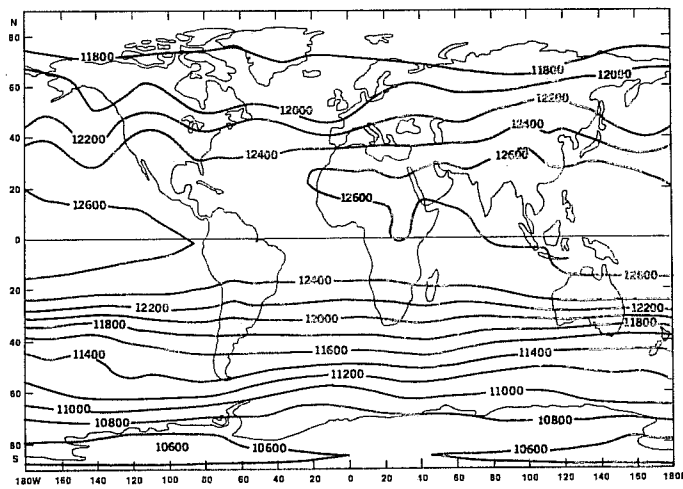

Figure 3.4b Simulated geopotential height (gpm) at 200 mb for July.

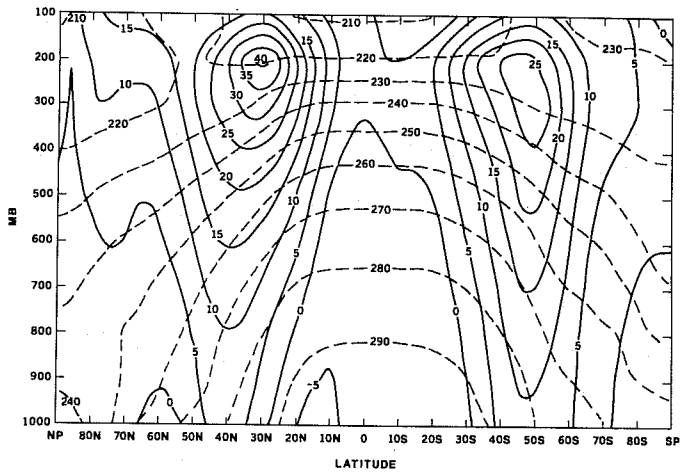

Figure 3.5a Observed zonally averaged zonal wind (ms^{-1}, solid lines) and temperature (K, dashed lines) for February, 1979.

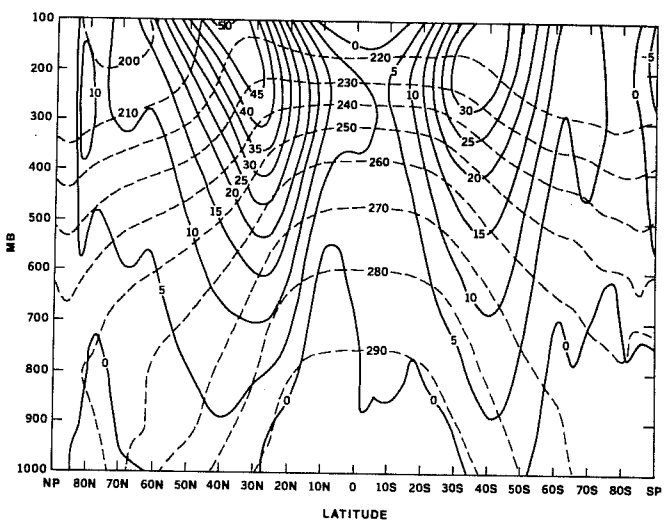

Figure 3.5b Simulated zonally averaged zonal wind (ms^{-1}, solid lines) and temperature (K, dashed lines) for February.

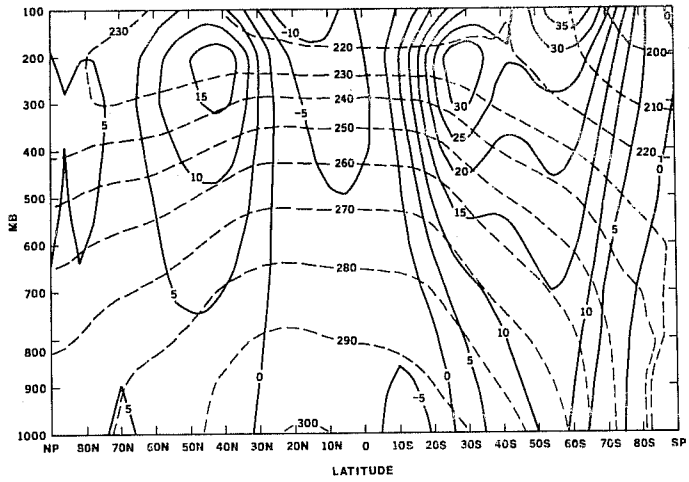

Figure 3.6a Observed zonally averaged mean zonal wind (ms^{-1}, solid lines) and temperature (K, dashed lines) for July, 1979.

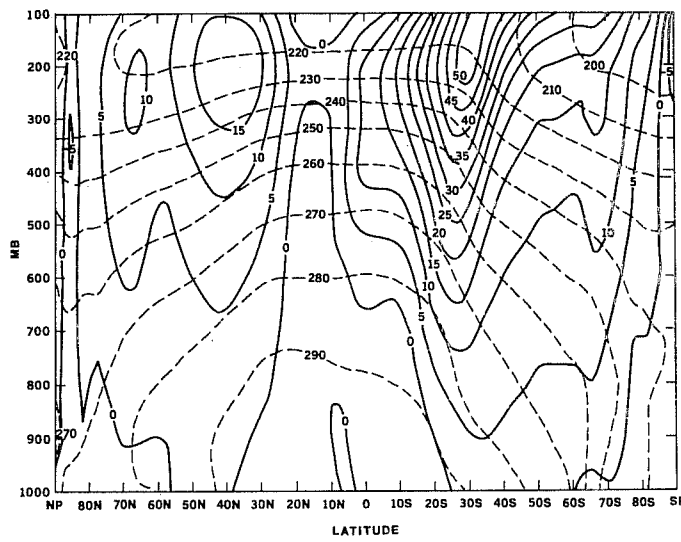

Figure 3.6b Simulated zonally averaged zonal wind (ms^{-1}, solid lines) and temperature (K, dashed lines) for July.

geopotential height field for winter (December, January, February) and summer (June, July, August), and Figures 3.3b and 3.4b show the corresponding simulation results for February and July respectively.

For February, the simulation of the trough over northeast North America, the ridge over the eastern Atlantic, and the jet stream over Japan are quite realistic. The ridge over the west coast of North America is displaced to the east. The simulation of the upper level anticyclonic circulation over the tropics is reasonable. The actual values of the geopotential, however, are substantially higher than the mean climatology. The southern hemispheric flow is also well simulated. The simulations show more distinct eddy structure in the southern hemispheric circumpolar flow along 40°-60°S.

For July, the simulated 200 mb flow shows large amplitude short waves over North America and the adjacent Pacific Ocean. The ridge over central North America is well simulated but the trough simulate off the west coast of North America is not present in the observed climatology. Although the local maximum associated with the Tibetan high is not well simulated, the large scale anticyclone over the Asiatic monsoon is reasonable. The geopotential height in the tropical belt is higher by about 200 gpm than climatology, due to an excessively warm simulated tropical atmosphere. The simulated location of the mid-Atlantic trough does not agree with the observations. The observed and simulated upper-level flows are both predominantly zonal in the Southern Hemisphere.

The surface circulation during July and the upper level circulation during January are, in general, better simulated than the surface circulation during winter and the upper level circulation during summer.

Figures 3.5a and 3.6a (solid lines) show the observed zonal wind for February and July 1979, and Figures 3.5b and 3.6b (solid lines) show the corresponding model simulations for February and July, respectively.

For February, the most conspicuous deficiency of the simulation is the absence of the closed maximum near 200 mb which is seen in the observations. The simulated zonal wind increases with height and tilts towards the north so that the model simulated zonal wind near the upper boundary is stronger than is observed. This deficiency is related to very low simulated temperatures in the upper tropospheric polar regions. The locations of the strongest zonal wind maxima in both hemispheres is fairly well simulated. The zonally averaged equatorial easterlies are a little too weak. The configuration of the zero wind line is not unreasonable except that it is too low south of the equator.

The dashed lines in Figures 3.5a and 3.5b show the zonally averaged temperature. The largest discrepancy is found near the upper boundary over the polar regions. Dynamical heat fluxes are not sufficient to compensate for the excessive radiative cooling associated with high level supersaturation clouds which are treated as black bodies. The middle troposphere over the polar regions is warmer than the observations. The simulated tropical atmosphere is considerably warmer than the observations.

For July, the observed and simulated zonal wind fields are in very good agreement, except that the jet in the Southern Hemisphere increases monotonically with height so that the maximum value occurs near the upper boundary. Zonally averaged temperatures (dashed line) near the northern pole are lower in the model simulations than in the observations. The simulated tropical atmosphere is again warmer than observations, and this may be one of the reasons for a stronger westerly jet in the Southern Hemisphere.

3.3 Fluctuations in space and time

The analysis presented in this sub-section was performed by D. Straus, of GLAS.

Figures 3.7 and 3.8 present the energy cycles of the simulated winter and summer seasons, and those estimated for the real atmosphere (Oort and Peixoto, 1974). Each energy cycle is computed in the space-time domain (Oort, 1964) and on a hemispheric basis. The observed energetics for January in the Northern

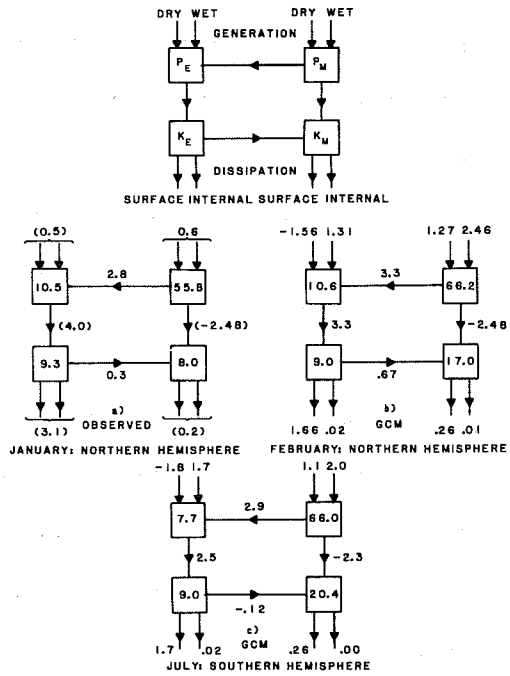

Figure 3.7 Energy cycles for the observed and simulated winter hemispheres, computed in the mixed space-time domain. P_M is the zonal-mean available potential energy, P_E the eddy available potential energy, K_E the eddy kinetic energy, and K_M the zonal-mean kinetic energy. The energies are quoted in units of 10^5 joules/m^2, the transformations and sources and sinks in units of watts/m^2. (a, left center) Observed Northern Hemisphere, January, (b, right center) GCM Northern Hemisphere, February, (c, lower) GCM Southern Hemisphere, July. (Values in parentheses are very approximate.)

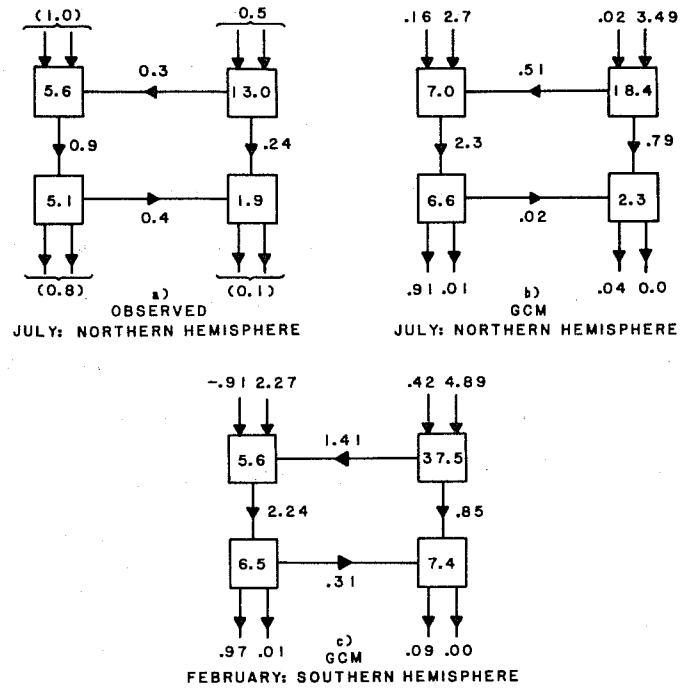

Figure 3.8 Energy cycles for the observed and simulated summer hemispheres, computed as in Figure 5.1. (a, upper left) Observed Northern Hemisphere, July, (b, upper right) GCM Northern Hemisphere, July, (c, lower) GCM Southern Hemisphere, February. (Values in parentheses are very approximate.)

Hemisphere (Figure 3.7a) indicate a strong (baroclinic) flow of energy from zonal available potential (P_M) to eddy available potential (P_E) to eddy kinetic (K_E) energy, and a weaker (barotropic) flow from eddy kinetic to zonal kinetic (K_M) energy. Also indicated is a conversion from K_M to P_M, although this estimate has a large degree of uncertainty associated with it (Oort and Peixoto, 1974). These energy transfers are reproduced remarkably well in the model Northern Hemisphere energy cycle for February (Figure 3.7b). The sizable conversion of K_M to P_M in the model suggests that the energy conversion of the thermally indirect Ferrel cell overcompensates that of the thermally direct Hadley cell. This is not inconsistent with the much larger mass flux associated with the Hadley cell, since the Ferrel cell exhibits a much larger temperature difference between the ascending and descending branches. The energy amounts in the model simulation agree well with the observations except for K_M; the fact that the model K_M is almost twice that of the observations is consistent with the model's unrealistically strong subtropical jet. Given the large uncertainties in estimating the generation and dissipation of energy in the real atmosphere (Oort and Peixoto, 1974), it is difficult to assess the model's performance with regard to these quantities. The dissipation of kinetic energy in the model's Northern Hemisphere (in winter) is within a factor of two of the observed estimate, with the model showing <u>less</u> dissipation of eddy kinetic energy than the observations. The model's winter generation of P_M (due to both dry and moist processes) is much stronger than the observed estimate. This may be due to excessive cooling near the winter pole and warming of the tropical atmosphere. The model also predicts a small net diabatic loss of P_E, in contrast with the estimate for the atmosphere.

The Southern Hemisphere energy cycle for the winter (July) simulation is indicated in Figure 3.7c, and it is seen to be quite similar to the simulated Northern Hemisphere winter cycle (Figure 3.7b). The only energy conversion which is substantially different is the barotropic conversion from K_E to K_M, which is of opposite sign in the two hemispheres. The energy sources and sinks are also qualitatively similar, and the zonal available potential and eddy

kinetic energies are close in magnitude. P_E is greater in the Northern Hemisphere, while K_M is greater in the Southern Hemisphere. The observed summer Northern Hemisphere energy cycle (July) is presented in Figure 3.8a. The baroclinic energy conversions, P_M to P_E and P_E to K_E, still have the same sense, although they are smaller than in January. The weak (barotropic) conversion from K_E to K_M is again present, but the estimate of the conversion between K_M and P_M has changed sign from the January observations. The amounts of the different types of energy are considerably less in summer than in winter. The energy conversions of the model Northern Hemisphere summer (July, Figure 3.8b) are in the same sense as observed, but they are generally of much larger magnitude. This is particularly true of the conversion from P_E to K_E. Furthermore, the amounts of energy in the model simulation are somewhat larger than observed, the discrepancy being the greatest for P_M. Frictional dissipation in the model is approximately the same as the observed estimate, but the total model generation of P_M and P_E greatly exceeds the estimates of the real atmosphere. In general, the simulated Northern Hemisphere summer circulation appears to be overly vigorous.

Comparing the model energy cycles for Northern Hemisphere summer (July, Figure 3.8b) and Southern Hemisphere summer (February, Figure 3.8c), it is seen that the conversions are generally similar in magnitude and are in the same direction. It should be noted, however, that the conversions P_M to P_E and K_E to K_M are larger in the Southern Hemisphere summer. Both hemispheres contain similar amounts of K_E and P_E, but the Southern Hemisphere K_M and P_M are significantly greater than those of the Northern Hemisphere. The sources and sinks of energy are comparable in the two summer hemispheres, although the generation of P_E by dry diabatic processes is of opposite sign.

We now discuss the meridional transports of sensible heat (internal energy), potential energy, kinetic energy, and the latent energy of condensation of water. These transports are time-averaged and vertically integrated, and are also divided into eddy and zonal-mean components.

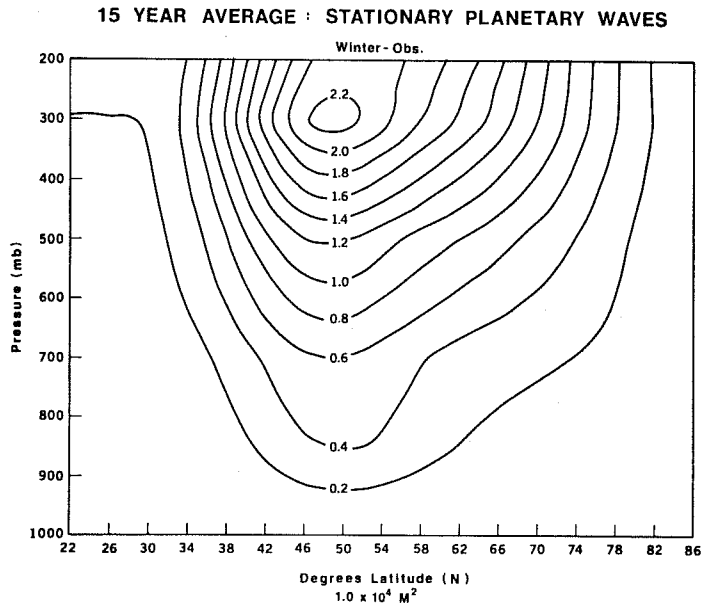

Figure 3.9a Observed winter stationary planetary wave variance of the geopotential height in the Northern Hemisphere. Units of 10^4 m^2.

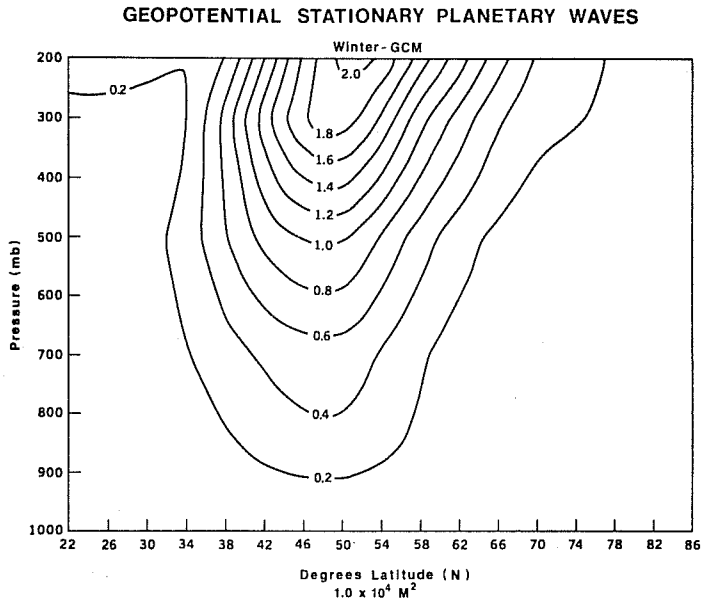

Figure 3.9b1 GCM winter stationary planetary wave variance of the geopotential height in the Northern Hemisphere. Units of 10^4 m^2.

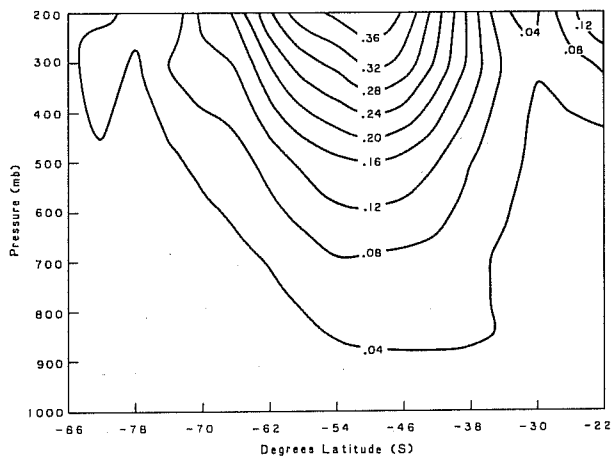

Figure 3.9b2 GCM winter stationary planetary wave variance of the geopotential height in the Southern Hemisphere. Units of 10^4 m^2.

The time-averaged departures from zonal symmetry of the basic meteorological fields reflect the lack of such symmetry at the lower boundary. That is, the presence of stationary waves is due to the existence of orography and geographically fixed, asymmetric heat sources. Thus, in order for a GCM to reproduce the observed three-dimensional structure of the stationary waves, the model must simulate the geographically fixed heat sources and flow over orography in a realistic manner.

We now present results for the stationary (time-averaged) component of the geopotential height, from which the stationary temperature and wind fields may be estimated by using hydrostatic and geostrophic balance respectively. Figure 3.9a shows the observed winter variance around a latitude circle of the stationary geopotential height, summed over the planetary waves (wavenumbers 1-4). The term "stationary" refers to a 90-day average commencing on January 1. This average was computed from NMC analyses for each of the years 1963-1977, and the mean over these years was taken. The corresponding stationary planetary wave variance for the winter GCM simulation is presented in Figure 3.9b1. "Stationary" here refers to a time-average over the first 90 days of the simulation, which was initialized from data valid for January 1, 1975. The model results show good overall agreement with the observations, with both variances reaching a maximum in the mid-latitude upper troposphere. The model variance is slightly too weak up to the 250 mb level, above which it fails to show the decrease with height apparent in the observations. This failure may be related to the unrealistically low polar temperatures and strong zonal winds at the upper levels. The model stationary planetary wave variance in the Southern (summer) Hemisphere (Figure 3.9b2) is almost an order of magnitude smaller than in the Northern Hemisphere, due to the relative lack of orography and geographically fixed heat sources in the Southern Hemisphere. It should be noted that the zonal variance of the stationary height field in the lowest four wavenumbers is (in winter) several orders of magnitude larger than the variance in higher wavenumbers, indicating that the total stationary variance will strongly resemble the planetary wave variance.

The observed summer variance of the stationary component of the geopotential height, summed over wavenumbers 1-4, is presented in Figure 3.10a. The corresponding GCM variance is shown in Figure 3.10b1. These quantities were computed in the same manner as for the winter season, except that the averaging period was defined to be the 90 days starting on June 15. (This time period was chosen to correspond to the summer simulation, which was initialized with data valid for June 15, 1979.) The simulated planetary wave variance agrees well with the observations with regard to the location and strength of the three maxima: one in mid-latitudes at about 300 mb, and two in the subtropics, at 850 mb and 200 mb. Discrepancies include the fact that the simulated mid-latitude variance does not decrease above 300 mb, the slight northward displacement in the GCM of the subtropical maximum at 850 mb, and the weakness of the simulated subtropical maximum at 200 mb. The Southern (winter) Hemisphere ultra-long wave variance (Figure 3.10b2) is now of the same order of magnitude as the Northern (summer) Hemisphere variance.

The band-pass RMS is closely associated with regions having a high frequency of cyclonic activity, and so indicates the location of the "storm tracks" (Blackmon et al., 1977). A comparison of the observed band pass RMS (Figure 3.11a) with that of the GCM (Figure 3.11b) shows excellent agreement in terms of both the location and strength of the major areas of cyclonic activity in the north central Pacific and western Atlantic.

The observed summer band-pass RMS height field (Figure 3.12a) shows the two oceanic maxima present on the winter map. The Atlantic maximum has been shifted to the east, and the magnitude of the summer RMS is generally much smaller. The corresponding (Northern Hemispheric) map for the GCM (Figure 3.12b) indicates that the Atlantic maximum has been realistically simulated, both with respect to position and to magnitude. The Pacific maximum, however, is too weak and is located too far to the west.

The analysis of meridional energy transports presented earlier indicated that the total vertically integrated northward transport of heat by the eddies was

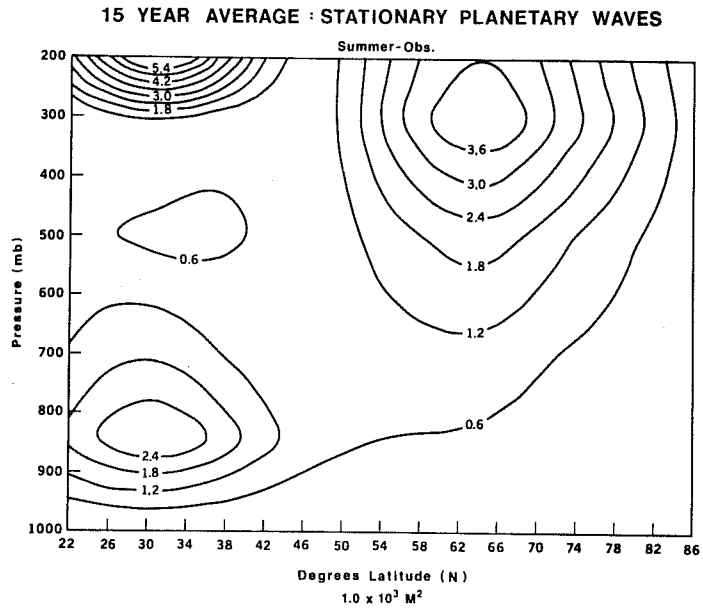

Figure 3.10a Observed summer stationary planetary wave variance of the geopotential height in the Northern Hemisphere. Units of 10^3 m^2.

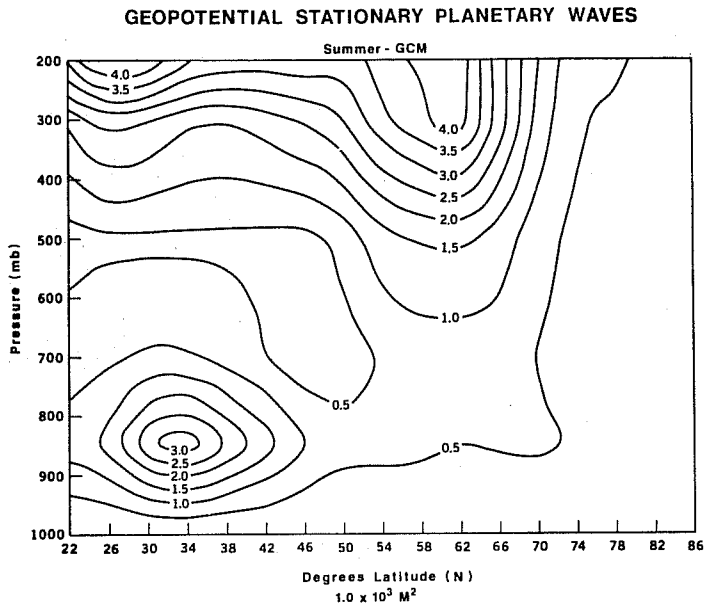

Figure 3.10b1 GCM summer stationary planetary wave variance of the geopotential height in the Northern Hemisphere. Units of 10^3 m^2.

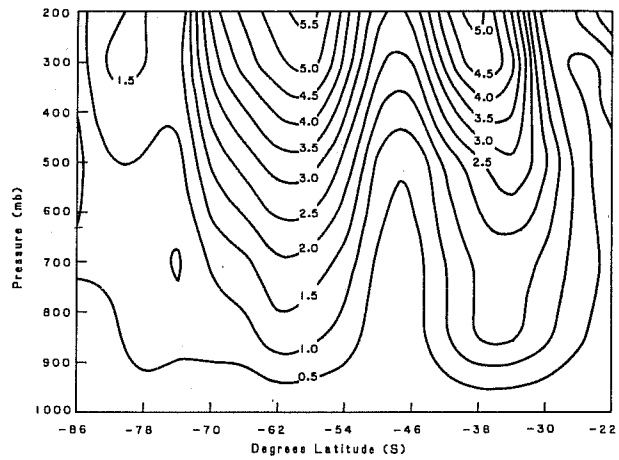

Figure 3.10b2 GCM summer stationary planetary wave variance of the geopotential height in the Southern Hemisphere. Units of 10^3 m^2.

Figure 3.11a Observed RMS deviation of the winter 500 mb band-pass geopotential height field (Northern Hemisphere), units of m. Contour interval is 5 m.

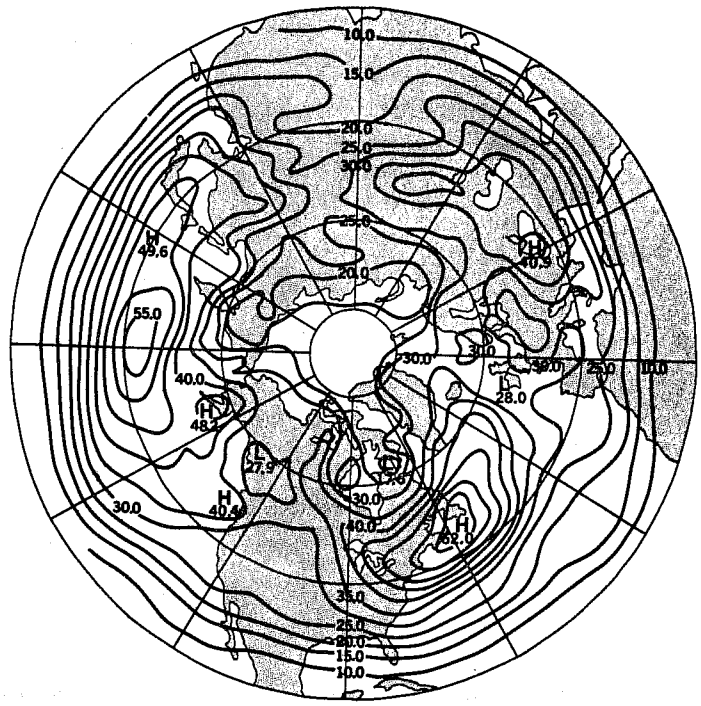

Figure 3.11b GCM RMS deviation of the winter 500 mb band-pass geopotential height field (Northern Hemisphere), units of m. Contour interval is 5 m.

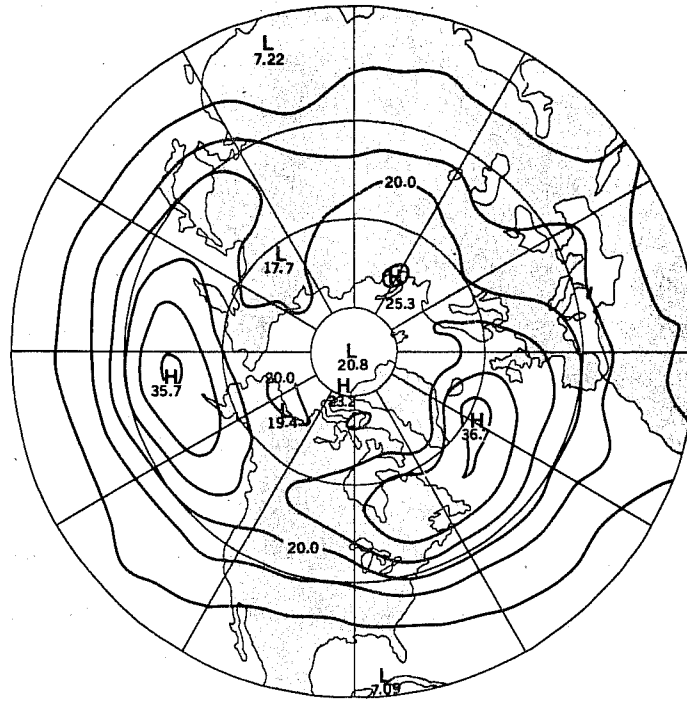

Figure 3.12a Observed RMS deviation of the summer band-pass 500 mb geopotential height field (Northern Hemisphere), units of m. Contour interval is 5 m.

Figure 3.12b GCM RMS deviation of the summer band-pass 500 mb geopotential height field (Northern Hemisphere), units of m. Contour interval is 5 m.

fairly realistic in both the winter and summer simulations. We now discuss latitude-height cross sections of both stationary and transient zonally-averaged meridional heat fluxes.

The observed (simulated) time mean February heat flux due to the stationary eddies is shown as a function of latitude and pressure level in Figure 3.13a (3.13b). The agreement between the model results and the observation is quite good. The observed midlatitude maximum of positive heat flux is well reproduced, as is the secondary maximum at 200 mb. Discrepancies include the presence of a sizeable negative heat flux in the model subtropics at 200 mb (which is not observed), the incorrect sign of the model heat flux north of 70N in the lower troposphere, and the slight equatorward displacement of the 200 mb maximum in the model results.

The time mean heat flux due to the transient eddies in February is given for the model in Figure 3.14b and for the observations in Figure 3.14a. No prefiltering of the data has been done before computing the transient component, so that this component includes a contribution due to the annual cycle. Both the observed broad maximum of positive flux in the mid-latitude lower troposphere and the weaker maximum near 200 mb are well reproduced by the model. Several differences exist, however. The region of large positive heat flux in the model penetrates higher than is observed, and the upper tropospheric maximum is unrealistically weak in the model.

The stationary eddy heat flux in July is very weak for both the model (Figure 3.15b) and the observations (Figure 3.15a). However, the model results show several features that are not observed, including maxima of negative flux in the subtropical lower troposphere, a maximum of positive flux at high latitudes in the lower troposphere, and a strong maximum of postive flux at the mid-latitude tropopause. The transient eddy heat flux in July, shown for the observations (model) in Figure 3.16a (3.16b), is much stronger. The model reproduces well the observed broad maximum of positive flux in mid-latitudes, although the peak

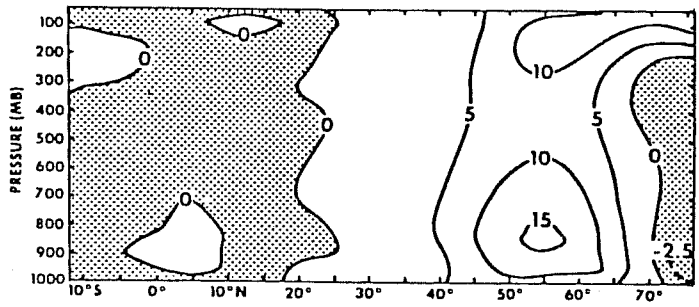

Figure 3.13a Observed February stationary eddy heat flux, in units of K m/sec.

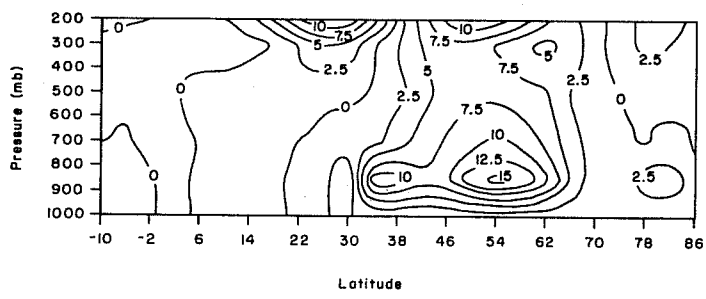

Figure 3.13b GCM February stationary eddy heat flux, in units of K m/sec.

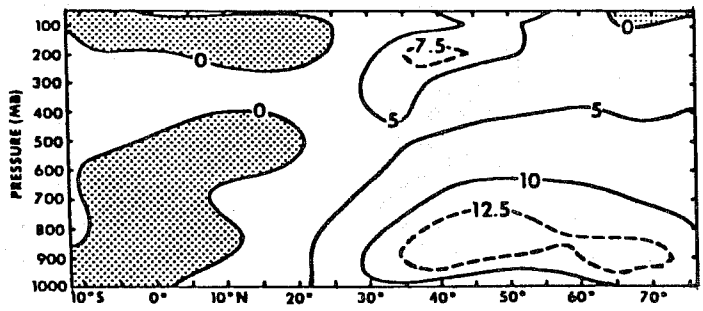

Figure 3.14a Observed February transient eddy heat flux, in units of K m/sec.

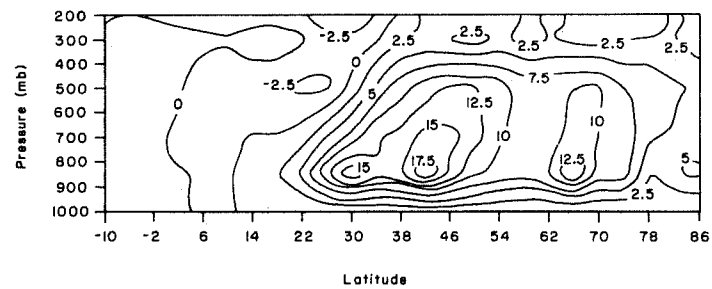

Figure 3.14b GCM February transient eddy heat flux, in units of K m/sec.

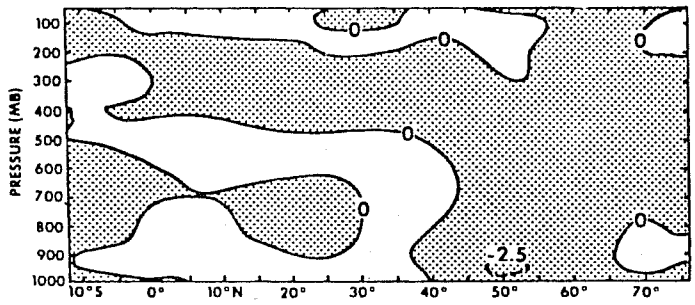

Figure 3.15a Observed July stationary eddy heat flux, in units of K m/sec.

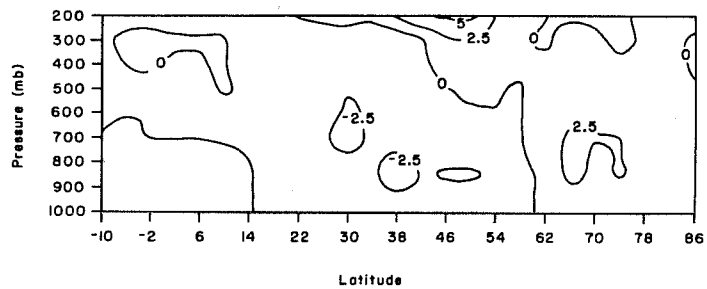

Figure 3.15b GCM July stationary heat flux, in units of K m/sec.

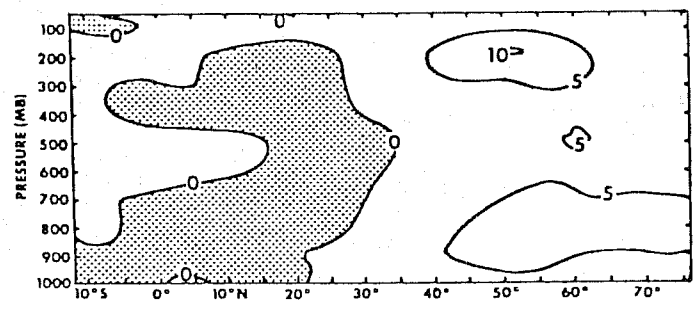

Figure 3.16a Observed July transient eddy heat flux, in units of K m/sec.

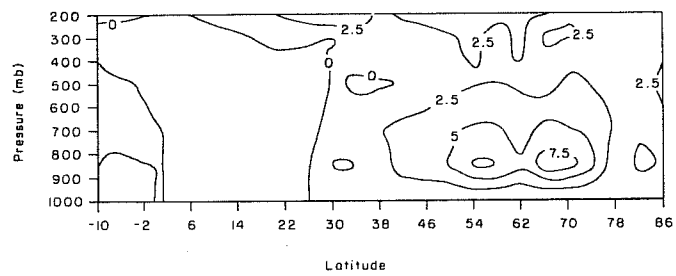

Figure 3.16b GCM July transient eddy heat flux, in units of of K m/sec.

values in the model seem slightly too large. Further, the maximum of positive flux near the tropopause in mid-latitudes is very weak in the model results.

The time mean momentum flux due to the stationary eddies in February is shown (as a function of latitude and pressure level) for the observations in Figure 3.17a, and for the GCM in Figure 3.17b. The observations are dominated by large positive (northward) values of the flux in the upper troposphere at mid-latitudes, and large negtive (southward) values farther north. The peak northward flux in the model upper troposphere in mid-latitudes is larger than observed, while the observed region of large southward flux is almost completely missing in the GCM results.

The observed time mean momentum flux due to transient eddies for February is shown in Figure 3.18a. It is dominated by a large peak in northward flux slightly north of 30N at the 200 mb level. The only other feature of note is the relatively small peak of negative (southward) flux at 200 mb at the equator. The model results (Figure 3.18b) also show a large maximum of positive flux, and its position is correct. However, it is too weak by a factor of two. A small maximum of southward flux at 200 mb over the equator is also present in the model, but it is too weak. A feature present in the GCM results which is not observed is the region of negative flux in the upper troposphere between 54 and 70N.

The behavior of the GCM's time mean momentum flux due to the stationary eddies for July is quite unrealistic (Figures 3.19a-b). The observations show a peak of northward flux at 200 mb at about 30N, while in the GCM results this peak is completely missing. The (small) maxima of negative flux in the model upper troposphere do not have their counterpart in the observations. In contrast to the stationary eddy flux of momentum, the model transient eddy flux of momentum behaves more realistically. The observations (Figure 3.20a) show three important features: a large maximum of positive flux at 200 mb at 45N, a smaller (positive) maximum at 200 mb just south of the equator, and a broad upper tropospheric maximum of negative flux north of 60N. The GCM results (Figure

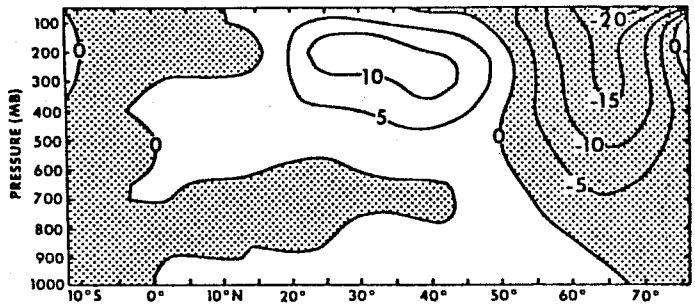

Figure 3.17a Observed February stationary eddy momentum flux, in units of $(m/sec)^2$.

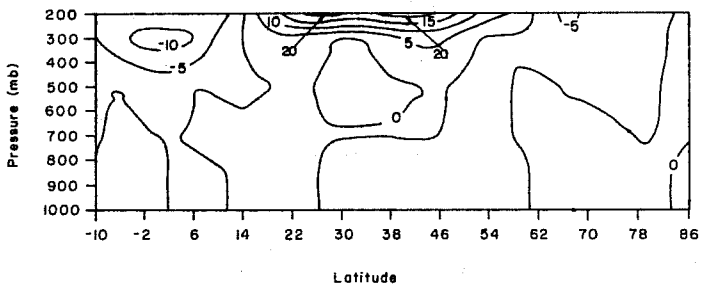

Figure 3.17b GCM February stationary eddy momentum flux, in units of $(m/sec)^2$.

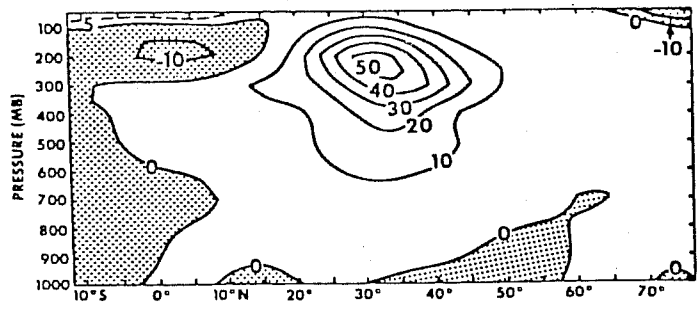

Figure 3.18a Observed February transient eddy momentum flux, in units of $(m/sec)^2$.

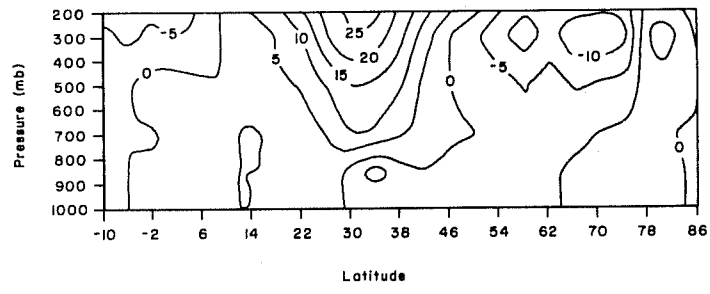

Figure 3.18b GCM February transient eddy momentum flux, in units of $(m/sec)^2$.

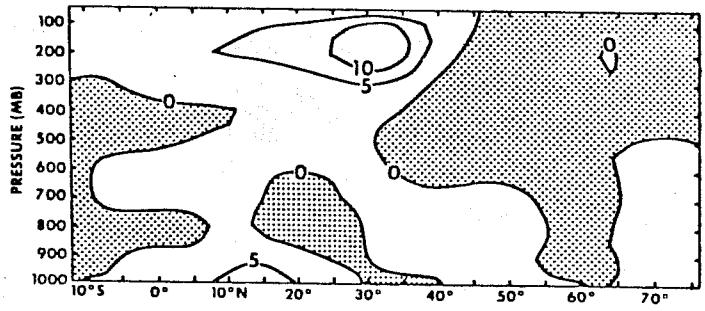

Figure 3.19a Observed July stationary eddy momentum flux, in units of $(m/sec)^2$.

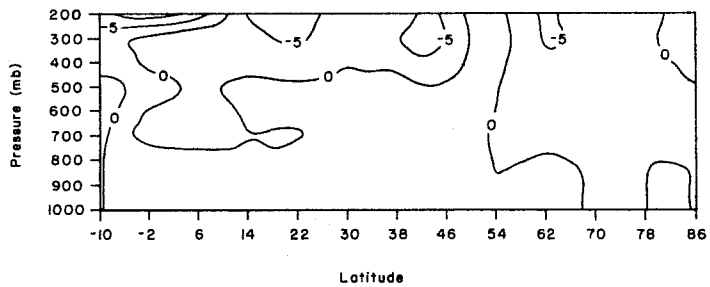

Figure 3.19b GCM July stationary eddy momentum flux, in units of $(m/sec)^2$.

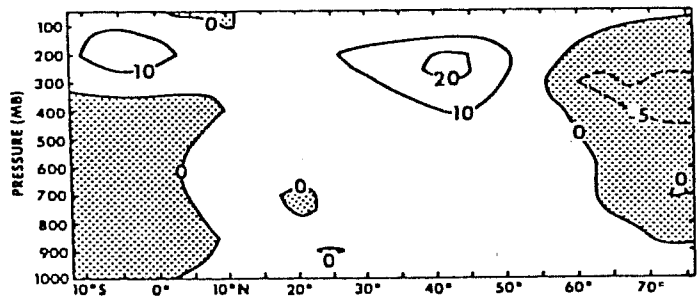

Figure 3.20a Observed July transient eddy momentum flux, in units of $(m/sec)^2$.

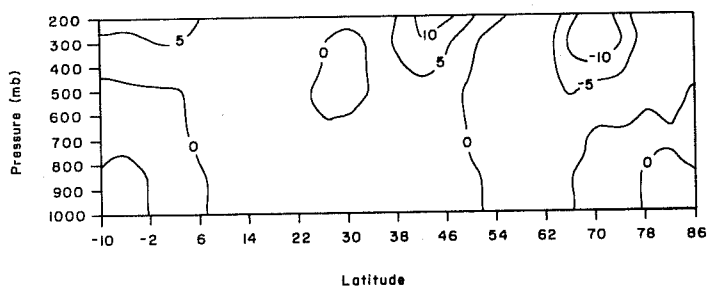

Figure 3.20b GCM July transient eddy momentum flux, in units of $(m/sec)^2$.

3.20b) show the same basic features, located approximately in the correct positions. However, the positive maxima are too small, and the negative maximum too large in magnitude.

3.4 Simulation of diabatic and frictional processes

Table 3.1 summarizes the global sensible heat and moisture budgets for the February and July simulations, giving the globally averaged surface sensible heat flux, evaporation, their ratio (termed the global Bowen ratio), the precipitation rate, and the planetary albedo. The observed surface fluxes are those of Budyko (1963) as given by Schutz and Gates (1971, 1972), the observed precipitation rates are from Jaeger (1976), and the observed planetary albedoes are from Raschke, et al. (1973). The simulated global mean evaporation and precipitation rates agree well with observations, and are improved relative to earlier versions of the model. The simulated surface sensible heat flux is also significantly improved, but it continues to be excessive. Finally, the simulated planetary albedoes are too high in both February and July, and are inferior to those obtained with earlier versions of the model.

The simulated and observed (Schutz and Gates, 1971, 1972) January/February and July zonal means of the evaporation are shown in Figs. 3.21a-b. In the February simulation, the evaporation maxima off the east coasts of Asia and North America have their observed magnitudes, although their shapes are not well-simulated and the secondary maximum south of Greenland is missed. The observed equatorial minimum is simulated in the Eastern Pacific, but is missed in Melanesia and the Indian Ocean. The zonal mean does not show the observed sharp equatorial mini mum. Observed maxima in the tropical South Atlantic, Indian, and South Eastern Pacific Oceans are either missing or weak and malformed.

Similarly, the simulated and observed (Schutz and Gates, 1971, 1972) surface sensible heat flux zonal means for January/February and July are shown in Figs. 3.22a-b. The February simulated surface sensible heat flux has maxima of the observed intensities off the east coasts of Asia and North America, but the Atlantic maximum fails to extend to the west coast of Scandinavia; it hugs the

Table 3.1

	Surface Sensible Heat Flux W m^{-2}	Surface Evaporation mm dy^{-1}	Global Bowen Ratio	Total Precipitation mm dy^{-1}	Planetary Albedo
Observed February	17.3	3.12	0.192	2.80	0.283
Simulated February	27.5	3.03	0.312	3.07	0.390
Observed July	20.7	3.28	0.218	2.84	0.281
Simulated July	32.5	3.22	0.347	3.24	0.380

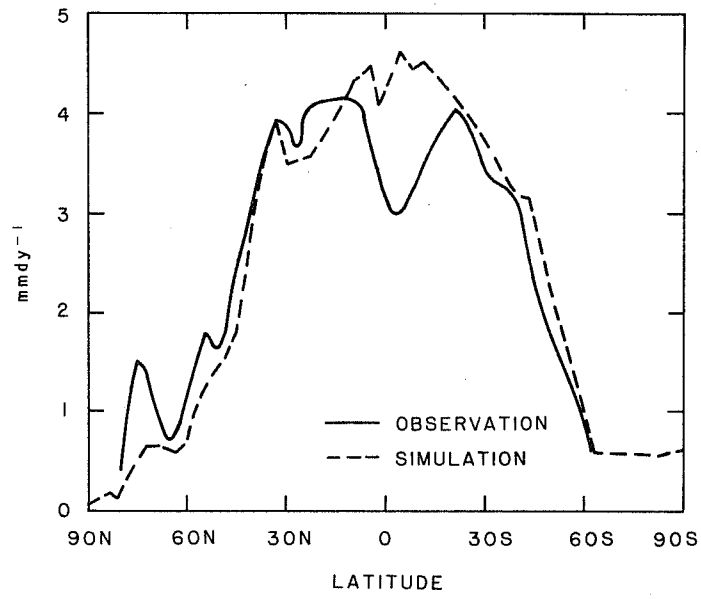

Figure 3.21a January observed zonal mean evaporation, mm dy^{-1}, taken from Schutz and Gates (1971) (solid line), and February simulated zonal mean evaporation, mm dy^{-1} (dashed line).

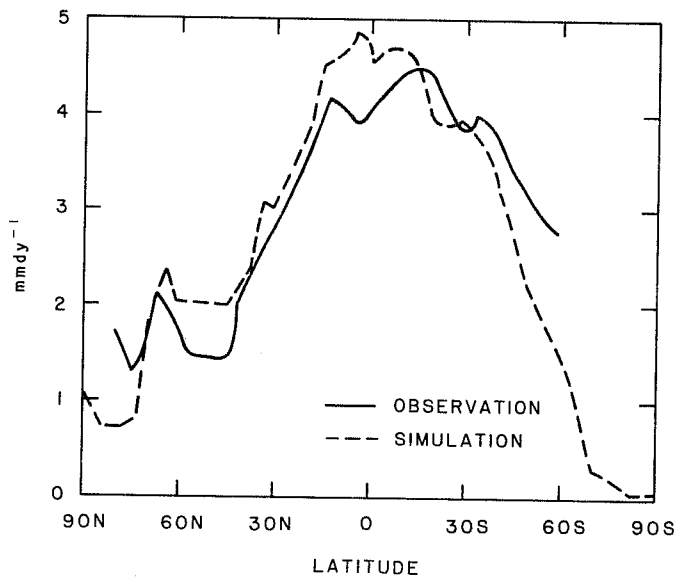

Figure 3.21b July observed zonal mean evaporation, mm dy^{-1}, taken from Schutz and Gates (1972) (solid line), and July simulated zonal mean evaporation, mm dy^{-1} (dashed line).

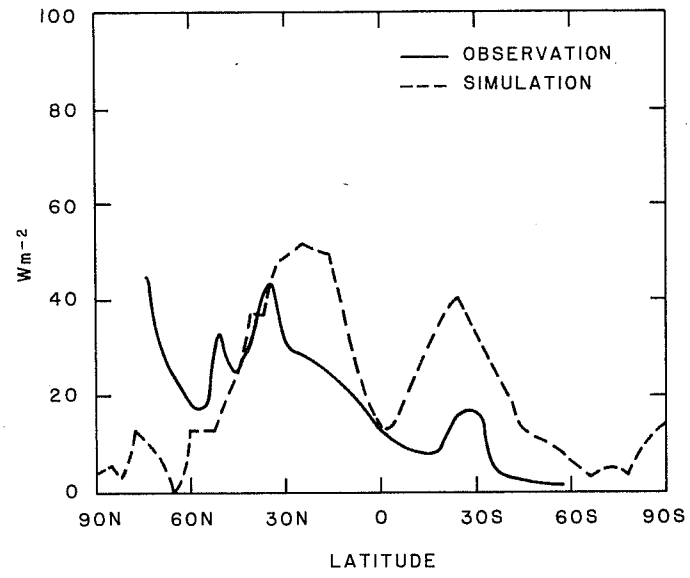

Figure 3.22a January observed zonal mean surface sensible heat flux taken from Schutz and Gates (1971) (solid line), and February simulated zonal mean surface sensible heat flux, Wm^{-2} (dashed line).

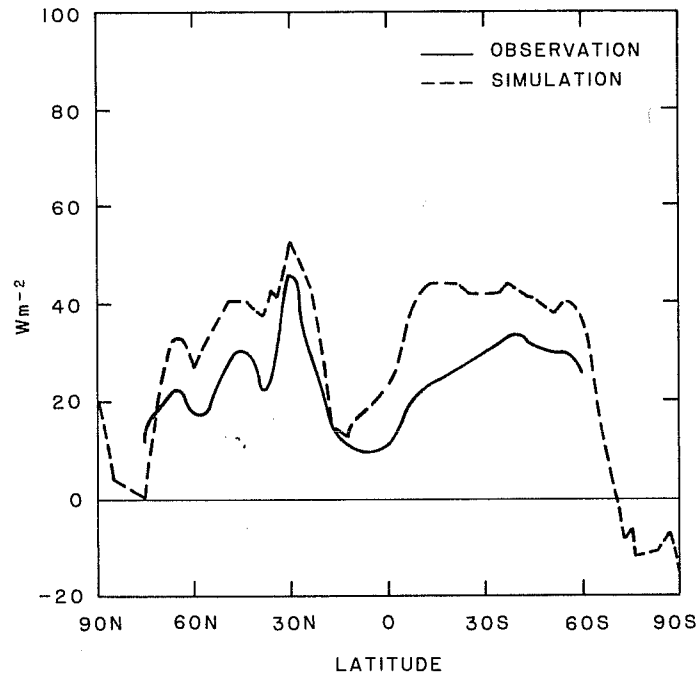

Figure 3.22b July observed zonal mean surface sensible heat flux taken from Schutz and Gates (1972) (solid line), and July simulated zonal mean surface sensible heat flux, W m^{-2}.

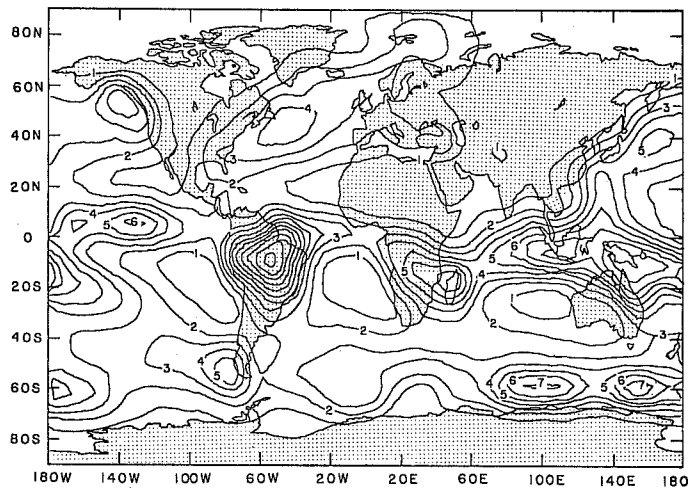

Figure 3.23a February observed precipitation, taken from Jaeger (1976). The contour interval is 1 mm dy^{-1}.

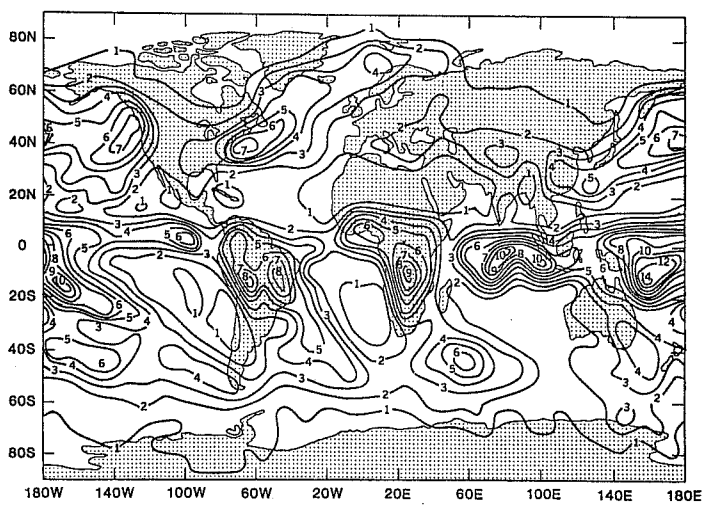

Figure 3.23b February simulated precipitation. The contour interval is 1 mm dy^{-1} except in congested regions.

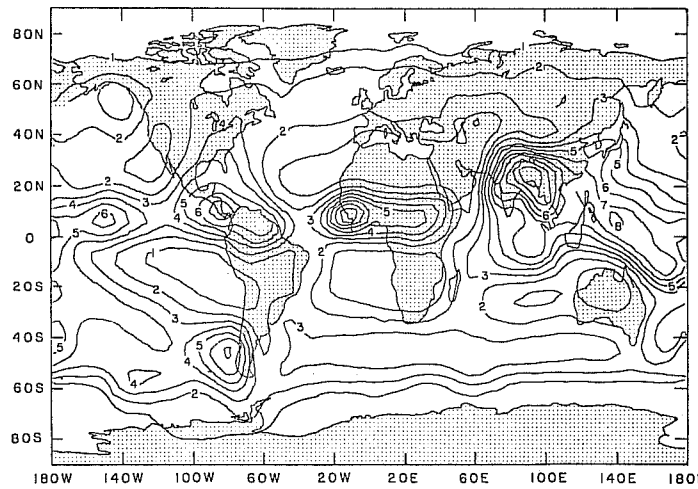

Figure 3.23c July observed precipitation, taken from Jaeger (1976). The contour interval is 1 mm dy^{-1}.

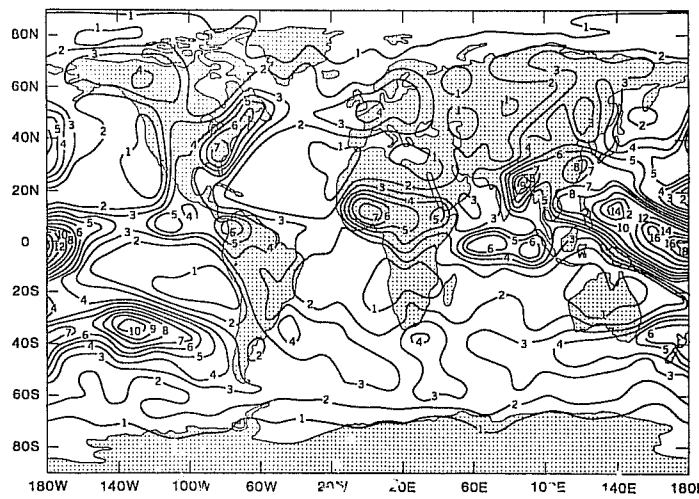

Figure 3.23d July simulated precipitation. The contour interval is 1 mm dy^{-1} except in congested regions.

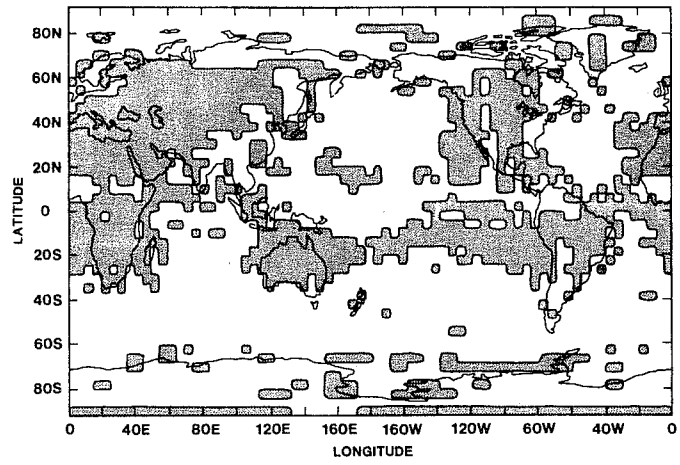

Figure 3.24a February simulated total cloudiness, in tenths. Regions with less than 7/10 cloudiness are shaded.

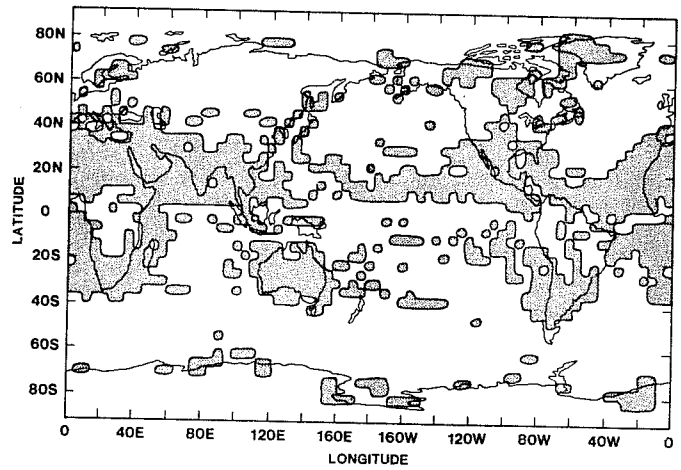

Figure 3.24b July simulated total cloudiness. Regions with less than 7/10 cloudiness are shaded.

coast of North America more closely than observed. The zonal mean of the simulated surface sensible heat flux is much stronger than observed. The simulated relative minimum at 10° north is about 20 W m^{-2}. The largest zonal mean values occur at 30° north, in both the simulation and the observations, but the simulated maximum is too strong.

The simulated and observed (Jaeger, 1976) February and July distributions of precipitation are shown in Fig. 3.23a-d. The simulated precipitation field is in excellent agreement with observations. Almost all important features are well-simulated in both position and intensity. Perhaps the single major discrepancy is the somewhat excessive (2 mm/day too large) February precipitation over the Tibetan plateau. In the July simulation the major monsoons are captured. The observed maximum over eastern North America is somewhat overpredicted.

The simulated February and July distributions of total cloudiness are shown in Fig. 3.24a-b. It is apparent that the simulated cloudiness is excessive. This is confirmed by the fact that the simulated planetary albedoes are too high (see again Table 3.1): the simulated February and July planetary albedos are 0.390 and 0.380, while the corresponding observed values (Raschke et al., 1973) are 0.283 and 0.281, respectively. Much of the excessive cloudiness is due to widespread "supersaturation" in the lowest model layer. Moeng and Randall (1982) show that even if cumulus cloudiness is completely neglected, the simulated albedo is practically unchanged. Apparently the boundary layer and cumulus parameterizations of the model do not allow realistic transport of moisture up out of the lowest model layer (Randall, 1982).

The model correctly simulates the seasonal increase in zonally-averaged except that the observed increase in Arctic cloudiness from February to July is missed. The cloudiness of the ITCZ is reasonably well-simulated, particularly for February, and the observed subtropical minima are also captured.

The simulated longitudinal distribution of cloudiness is much less satisfactory. The observed subtropical July maxima off the west coasts of North America,

South America, and South Africa are not only missed; they are replaced by minima. The observed maxima are known to be associated with stratus and stratocumulus clouds within the planetary boundary layer. The fact that the model has not simulated these maxima indicates that an improved planetary boundary layer parameterization is needed (Randall, 1982).

4. 1982 MODEL DESCRIPTION AND BOUNDARY CONDITIONS

The past two years have seen major improvements in model performance, as a result of several revisions of the model's numerical schemes and physical parameterizations. The principle changes to the model are:

1. New boundary layer parameterization.
2. New parameterization of evapotranspiration from land surfaces.
3. New parameterization of the interaction between clouds and radiation.
4. New scheme to maintain computational stability near the poles.
5. New vertical differencing scheme.
6. New tape format.
7. New postprocessing package.

The model code has been completely rewritten for improved speed and readability, and we have produced a comprehensive documentation (Randall et al., 1982a,b,c; Krishnamurthy, 1982; Davies, 1982). The model is running on the new Cyber 205 computer at GLAS. It uses approximately 3 cpu minutes per simulated day.

Randall (1982) has described the new planetary boundary layer parameterization, and has assessed the resulting changes in model performance. The sea level pressure distribution is considerably improved over the earlier model results, mainly because the new parameterization predicts lower surface stresses over the ocean. The global maps of the surface fluxes are generally smoother and more orderly with the new parameterization.

The rate of evapotranspiration from a land surface depends on the wetness and temperature of the surface, as well as the turbulent boundary layer processes in

the atmosphere above. We assume that the evapotranspiration rate E is given by

$$E = \beta E_p \quad , \tag{4.1}$$

where β is a measure of the surface wetness, and E_p is the potential evapotranspiration. This assumption has also been used in earlier versions of our model. However, following suggestions of Professor Y. Mintz (personal communication, 1981) we have adopted new definitions of E_p and β. Previously, E_p was computed using the predicted ground temperature. Now, however, we compute E_p using a saturated lysimeter temperature, which we have introduced into the model as a new prognostic variable. The form of β has been modified accordingly. A brief discussion of the motives for these changes is given below.

Davies and Allen (1973) measured the daily mean evapotranspiration from two neighboring rye-grass plots. One plot was kept saturated, so that the evapotranspiration from that plot was approximately equal to the potential evapotranspiration for the temperature of the plot. The second plot was allowed to be wet or dry according to the vagaries of the weather. For both plots, Davies and Allen measured the volumetric soil moisture content and evaporation rate. Nappo (1975) used the same data set to relate the ratio of the evaporation rates from the two plots to the volumetric moisture content of the nonirrigated plot.

Mintz and Serafini (1981, hereafter MS) used the Davies-Allen data to show how the ratio of the two evaporations is related to the ratio of the volumetric moisture contents. MS argued that the ratio of the volumetric soil moistures is approximately equal to w/w_*, where w is the moisture content of the soil layer extending from the surface down to the effective root depth, and w_* is the value of w corresponding to complete saturation of this layer. Specifically, MS proposed that

$$\beta = 1 - \exp(-6.8\, w/w_*) \quad . \tag{4.2}$$

Because (4.2) is based on the Davies-Allen data, we must adopt a definition of E_p which is consistent with that data. Therefore, we must compute E_p, for each grid box, using the temperature of a saturated plot within the grid box. The

plot is assumed to be small enough so as not to directly affect averages over the box, and it is assumed to experience the same sunshine, cloudiness, and turbulent forcing as the grid box as a whole. The temperature of the saturated plot is carried as a prognostic variable.

Randall (1983) has performed a simulation experiment to assess the change in model performance obtained with the new evapotranspiration parameterization. In the control run, the potential evapotranspiration was obtained using the saturated lysimeter temperature, while in the experiment it was obtained using the predicted ground temperature for the grid box as a whole. The two runs were initialized with the observed state of the atmosphere for June 15, 1979, and integrated through the end of July. The July mean results show that, as expected, the use of the lysimeter temperature leads to a considerable reduction (i.e., improvement) in the evaporation over the subtropical deserts, such as North Africa and the southwestern United States. The ground temperature increases in these regions, but there is little change in the surface sensible heat flux, because the PBL air temperature also increases. The net radiation flux out of the surface increases enough to compensate for the reduced evaporation. The time-averaged difference between the lysimeter temperature and the ground temperature is small except in desert regions; in the Sahara it approaches 20°C.

We have made two changes in the model's parameterization of the interaction between clouds and radiation. First, we have made all clouds in the top three layers of the model transparent with respect to both solar and terrestrial radiation. Previously, clouds in these layers were assumed to interact strongly with both radiation streams. (The latent heating and drying due to large-scale saturation in the top three layers is still computed as before. Cumulus clouds have never been permitted to penetrate into these layers.) This change was motivated by a suspicion that excessive radiative cooling due to high-level clouds was partly responsible for the excessively cold polar upper troposphere in the simulations reported by Shukla et al. (1981). A 30-day test run showed

that the polar cooling has been reduced somewhat in the revised model, although the problem has not been solved by any means. The second change to the cloudiness parameterization is that the fractional cloudiness due to cumulus clouds is now neglected. Previously, these clouds were assumed to produce 100% fractional cloudiness, which is very unrealistic. Moeng and Randall (1982) showed that neglect of the radiative effects of cumulus cloudiness leads to improved solar and terrestrial radiation distributions in a July simulation.

As discussed in Section 2, the earlier version of the model used a "split grid" in which the number of grid points around a latitude circle was decreased near the poles. We have abandoned this scheme in favor of the original Arakawa B-grid (Arakawa and Lamb, 1977), for the following reasons:

1) Model results showed that significant computational noise was generated in the split grid region.

2) Code associated with the split grid made the model program listing very unwieldy and difficult to understand.

3) Execution of split grid code significantly slows model performance, especially on vector machines.

With or without the split grid, it is necessary to filter selected fields in the longitudinal direction near the poles in order to maintain computational stability. In the earlier versions of the model, the filter consisted of a 3-point smoother applied repeatedly. The number of repetitions increased towards the pole. The design of this filtering procedure is inadequately documented in the literature. Tests performed with a B-grid shallow water model showed that smoother solutions are obtained with a Fourier filter based on the design of Arakawa and Lamb (1977). In the present climate model, this Fourier filter is applied to the zonal wind which is used to compute the zonal mass flux, and to the zonal component of the pressure gradient force. (The prognostic fields themselves are not Fourier filtered.)

We have adopted a vertical differencing scheme based on the work of Arakawa and Lamb (1977) and Arakawa and Suarez (1982). The vertical advection of moisture is done in such a way as to avoid the computational moist convective instability which Arakawa calls "Conditional Instability of a Computational Kind" (CICK).

The model history tape is the primary record of a simulation. It also makes it possible to restart the model from any one of many records on the tape, the first of which is the initial condition. The tape contains a copy of the actual model code used in the simulation, as well as the boundary condition data sets. Finally, it contains a very detailed record of the simulation for a few dozen selected grid points. Three "reference files" are written at the start of the first tape of the run. The first file contains the source code for the model. The second contains copies of the boundary conditions (topography, sea surface temperature, and albedo) used. The third contains input data required by the long wave radiation parameterization. Extensive data is recorded in "grid-point history files," for selected grid points. These files are written every call to physics, so they contain a very complete record of the simulation for the points selected. The number and choice of points in the file has been left flexible. A reasonable number of points is 50. Finally, "synoptic files" are written, typically every 12 hours. Each of these files contains the instantaneous global distributions of the prognostic variables, as well as a wide variety of diagnostic output variables, averaged over the time-interval since the preceding synoptic record.

A completely new postprocessing package has been designed to aid in the study of the model results. The synoptic records described above are written to tape in sigma coordinates. A program has been created to read one or more of these σ-history records, interpolate to constant pressure surfaces, and write the results to tape. Another program is used to create tapes containing time-averages of these pressure history tapes. Utilities have been developed to create tapes recording the difference between two time-average tapes. An elaborate plot package has been developed to generate plots of individual pressure history

records, time averages, or differences between time averages. Finally, grid-point history records can be sorted by grid point, and plotted as simple plots against time (e.g., the record of precipitation at a grid point) or as time-height contour plots (e.g., of total diabatic heating). All tapes are catalogued using naming conventions that document the experiment number, type of data, time-interval included, etc.

Two changes were made to the boundary conditions for this run. First, the topography was revised to assign more realistic heights to Greenland. Second, the seasonally varying ground wetness data of Mintz and Serafini (1981) was included as an additional boundary condition, i.e., the ground wetness was made non-interactive.

5. SEASONAL SIMULATION

5.1 Initial conditions

The model was initialized with the observed state of the atmosphere for 00Z, November 15, 1978. The initial ground temperatures for both the grid box and the small saturated plot were assumed to be equal to the surface air temperature. The initial snow boundaries were obtained from the climatological data of Matson (1977), and the initial snow depths were specified as functions of the surface albedo.

5.2 Results

Here we present some monthly-mean results for January and July. The January mean starts one and a half months after initialization, and the July mean starts seven and a half months after initialization.

Fig. 5.1a shows the simulated January sea level pressure distribution, which can be compared with the January observations of Fig. 3.1a, and with the earlier February simulation (with the 1980 model) shown in Fig. 3.1b. The new simulation is clearly superior in many respects. The Siberian High is stronger, the Icelandic Low is deeper, the trough of the "roaring 50's" around Antarctica is much deeper and more realistic, and the subtropical highs of the Southern

a)

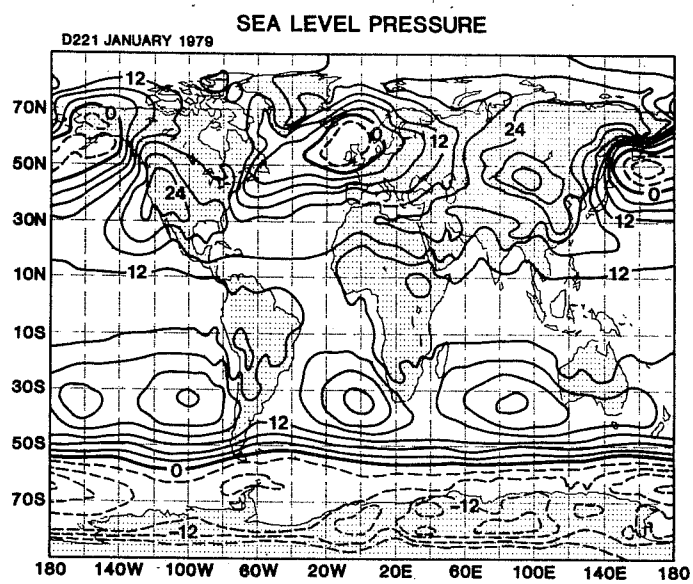

b)

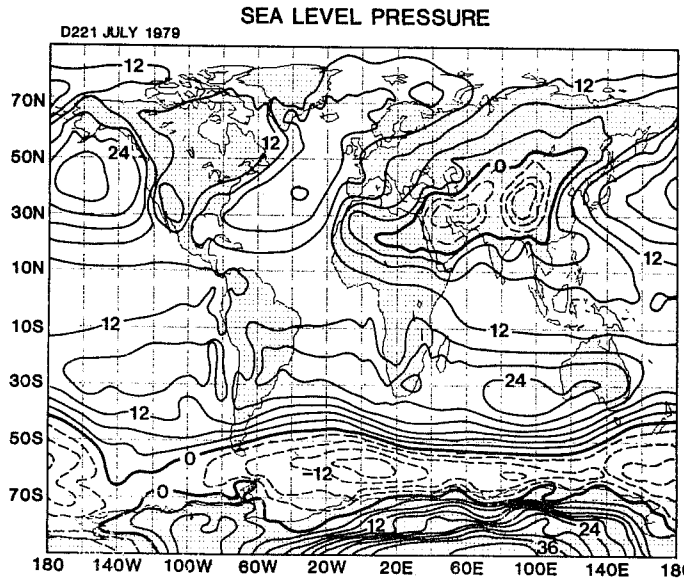

Figure 5.1 Simulated sea level pressure distributions for (a, upper) January, and (b, lower) July, obtained with the 1982 model. A thousand mb has been subtracted everywhere. The 0 contour (1000 mb) is heavy, and negative contours are dashed. The contour interval is 4 mb.

a)

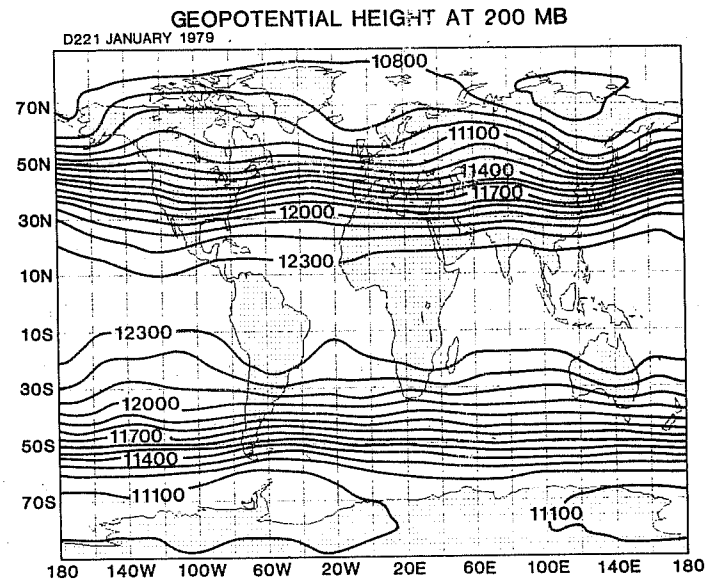

b)

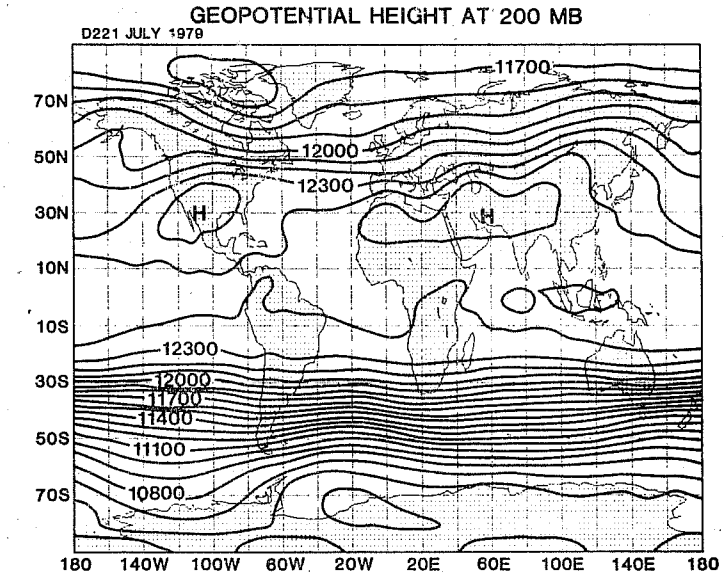

Figure 5.2 Simulated 200 mb geopotential height for (a, upper) January, and (b, lower) July. The units are meters, and the contour interval is 100 m.

Hemisphere are stronger and better organized. As discussed by Randall (1982), to a large extent these improvements and the result of the new PBL parameterization, which produces lower surface drag coefficients and so allows sharper features in the sea level pressure pattern.

Fig. 5.1b shows the simulated July sea level pressure distribution, which can be compared with the July observations of Fig. 3.2a, and with the earlier July simulation (with the 1980 model) shown in Fig. 3.2b. The thermal lows over southern Asia and southwestern North America are well simulated, and the Antarctic circumpolar trough is again much improved over the 1980 model results. The Atlantic High in the Northern Hemisphere is elongated from southwest to northeast; other July simulations with the same model have produced more cellular highs. The subtropical highs of the Southern Hemisphere are almost as strong as observed, in the zonal mean; however, the shapes of the individual highs are not well simulated.

Fig. 5.2a shows the simulated January 200 mb geopotential height field. This can be compared with the observed December-January-February distribution in Fig. 3.3a, and with the earlier February simulation (with the 1980 model) shown in Fig. 3.3b. The primary improvement with respect to the earlier results is that the tropical heights are now realistic, whereas earlier they were about 200 m too high. Although we have not as yet pinned down the reason for this improvement, it appears to be related to the new vertical differencing scheme, and/or to the neglect of cloudiness in the top three model layers. In the Northern Hemisphere, the prominent troughs and ridges of the long waves are somewhat weaker than observed, and are displaced towards the east with respect to observations. This may be related to the excessively strong winter westerlies, which still plague the model.

Fig. 5.2b shows the simulated July 200 mb geopotential height field. This can be compared with the observed June-July-August distribution in Fig. 3.4a, and with the earlier February simulation (with the 1980 model) shown in Fig. 3.3b. Again, the new model produces more realistic tropical heights. The highs over

Central America and Southern Asia are well simulated, although the latter is displaced to the west.

The simulated January zonally averaged zonal wind and temperature are shown in Fig. 5.3a. This can be compared with the February observations of Fig. 3.5a, and with the earlier February simulation (with the 1980 model) shown in Fig. 3.5b. The simulated low-level tropical easterlies are realistically deep in the Southern Hemisphere, and realistically strong at 10°N. In comparison with the earlier model, the excessively strong winter westerlies are somewhat improved, but they continue to be unrealistic. The improvement is associated with a cooling of the tropics rather than a warming of the poles. The latitude of the simulated summer hemisphere jet is more realistic in the new model.

The simulated July zonally averaged zonal wind and temperature are shown in Fig. 5.3b; the corresponding observations are given in Fig. 3.6a, and the results from the 1980 model are given in Fig. 3.6b. The new model produces tropical easterlies at all levels, and a low-level easterly maximum at 10°S, in agreement with observations. The excessively strong winter westerlies show little improvement in comparison with the 1980 model. The northern summer jet is not as well simulated in the new model.

Figs. 5.4a and b show the observed and simulated January precipitation distributions, respectively. For comparison the February precipitation given by the 1980 model is shown in Fig. 3.23a. The overall pattern of simulated precipitation is quite realistic, although the rain belt over Africa is too far north. The simulated maxima near 60°S may be realistic; the observations are particularly questionable in that region. The simulated global mean is substantially larger than observed.

Figs. 5.5a and b show the observed and simulated July precipitation distributions, respectively. The corresponding results from the 1980 model are given in Fig. 3.23d. Again, the African rain belt is too far north. The precipitation maximum over eastern North America is overpredicted, and there is too much

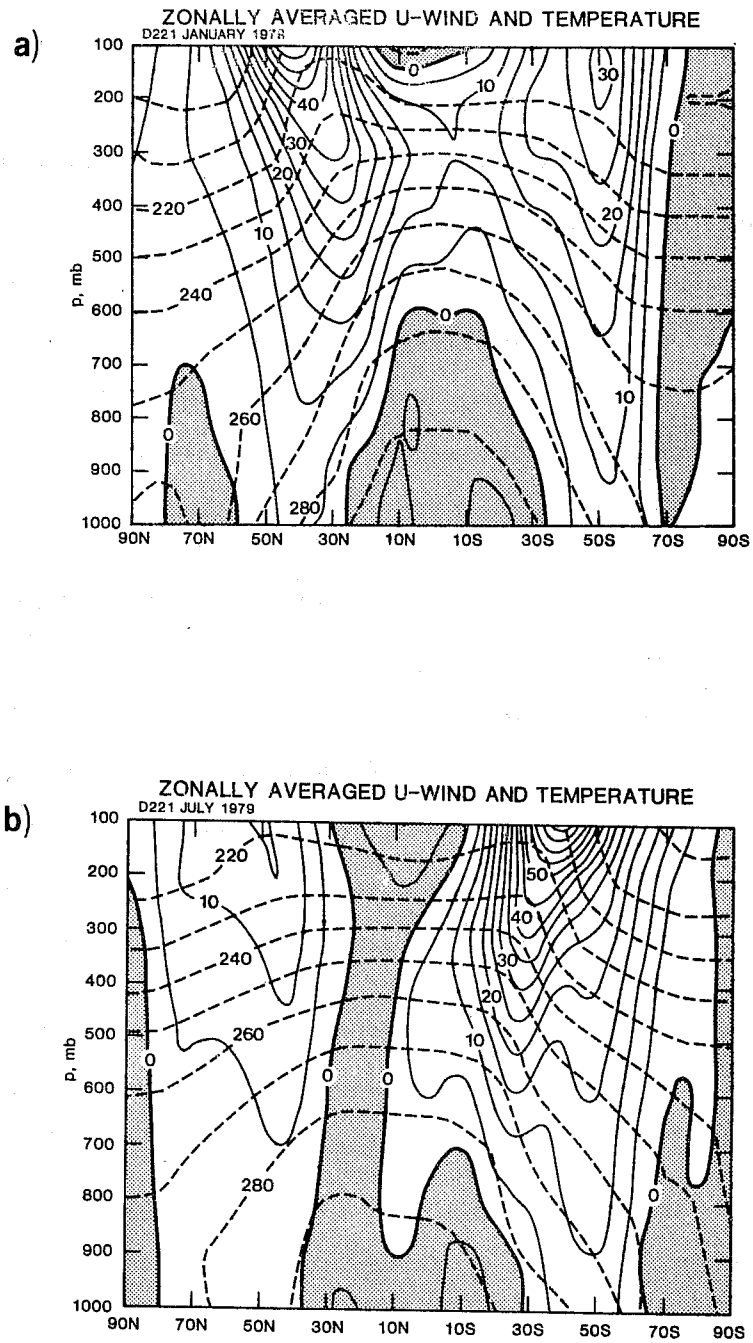

Figure 5.3 Simulated zonally-averaged zonal wind (solid contours) and temperature (dashed contours) for (a, upper) January, and (b, lower) July. Regions of easterlies are shaded.

a)

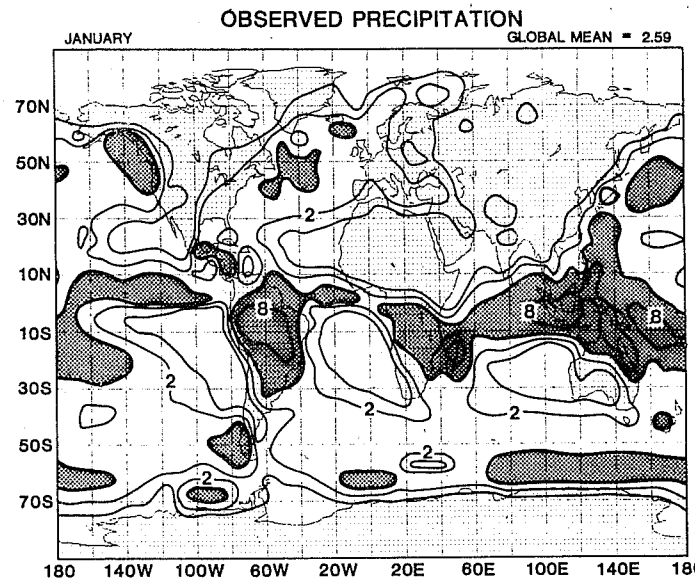

b)

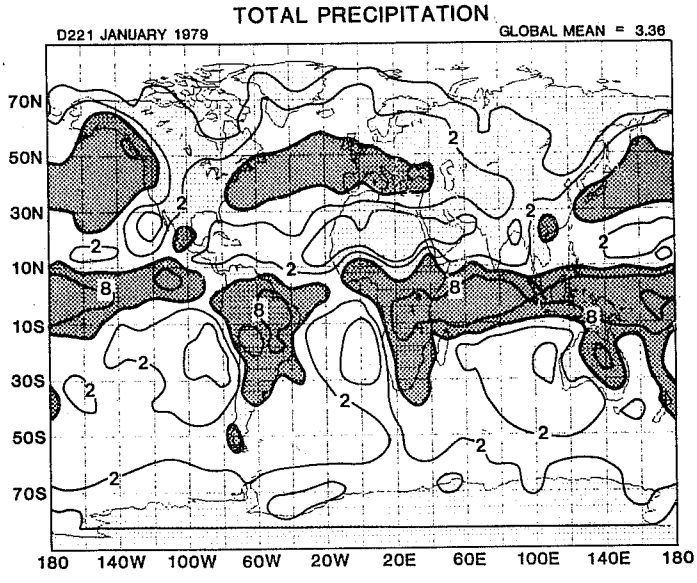

Figure 5.4 Global distribution of precipitation, in mm day^{-1}, for (a, upper) observed January, (b, lower) simulated January. Values in excess of 4 mm day^{-1} are shaded. The contours plotted are 1, 2, 4, 8.

a)

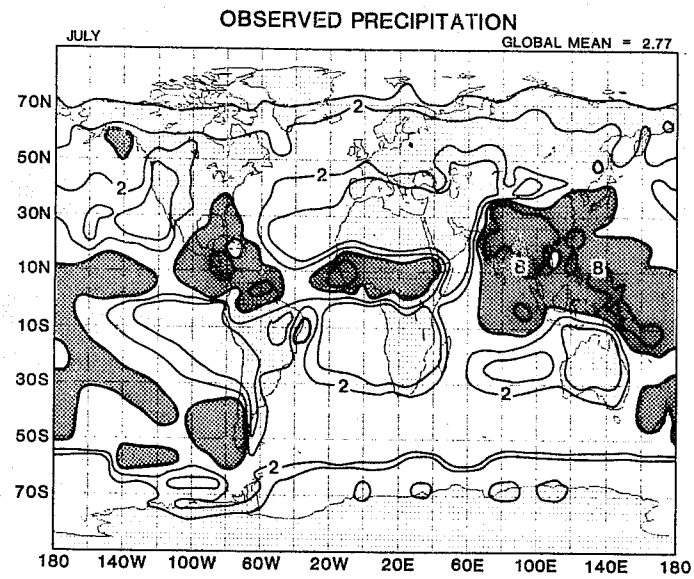

b)

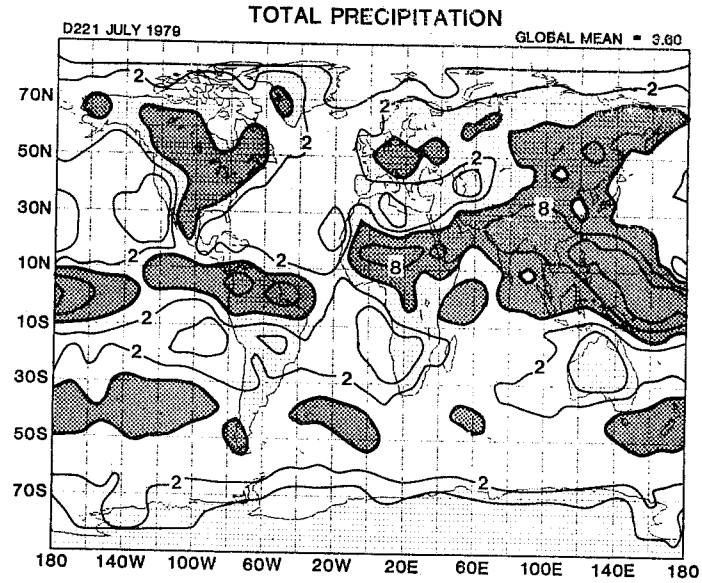

Figure 5.5 Global distribution of precipitation, in mm day^{-1}, for (a, upper) observed July, (b, lower) simulated July. Values in excess of 4 mm day^{-1} are shaded. The contours plotted are 1, 2, 4, 8.

rain over northeastern Asia. In general, there is too much precipitation over land. This may indicate a need for further revision of the ground hydrology parameterization.

6. CONCLUDING REMARKS

The GLAS climate model is an evolving simulation tool. An extensive study of model results has shown that the model can realistically simulate many observed aspects of the earth's climate, including quasi-stationary large-scale circulation patterns, space-time variability, and the hydrological cycle. Recent revisions of the model design have led to significant improvements in performance, particularly in the simulation of sea level pressure and the thermal structure in the tropics. These improvements were made possible mainly by revisions of the parameterizations of the planetary boundary layer and the interaction of clouds with radiation. The most recent version of the model has demonstrated its ability to simulate seasonal transitions. In the near future, we plan to exploit our recently expanded computing capability to study interannual variability, as well as to increase the model's resolution and raise the model top to include the stratosphere.

7. ACKNOWLEDGEMENTS

This work has been performed in collaboration with J. Shukla, D. Straus, and Y. Sud of GLAS, and L. Marx, and J. Abeles of MACOM/Sigma Data Corporation. I am grateful to ECMWF for making my participation in this workshop possible.

8. REFERENCES

Arakawa, A., 1969: Parameterization of cumulus convection. Proc. WMO/IUGG Symposium on Numerical Prediction in Tokyo, IV8, 1-6.

Arakawa, A., 1972: Design of the UCLA General Circulation Model. Numerical Simulation of Weather and Climate, Technical Report No. 7, Dept. Meteorology, UCLA.

Arakawa, A., and V. R. Lamb, 1977: Computational design of the basic dynamical processes of the UCLA general circulation model. Methods in Computational Physics, 17, Academic Press, New York, 173-265.

Blackmon, M. L., J. M. Wallace, N. C. Lau and S. L. Mullen, 1977: An observational study of the Northern Hemisphere wintertime circulation. J. Atmos. Sci., 34, 1040-1053.

British Meteorological Office, 1977 "Monthly Ice Charts", Meteorological Office, London Road, Bracknell, Berkshire.

Crutcher, H. L., and O. M. Davis, 1969: U.S. Navy Marine Climatic Atlas of the World. NAVAIR 50-1C-54, Naval Weather Service Command, Washington, D.C.

Davies, J. A., and C. D. Allen, 1973: Equilibrium, potential, and actual evaporation from cropped surfaces in southern Ontario. J. Appl. Meceor., 12, 649-657.

Davies, R., 1982: Documentation of the solar radiation code in the GLAS GCM. NASA Tech. Memo. 83961, 57 pp.

Godbole, R. V., and J. Shukla, 1981: Global analysis of January and July Sea Level Pressure. NASA Tech. Memo. 82097.

Halem, M., and G. Russell, 1973: A split-grid differencing scheme for the GISS model. Research Review, 1973, (Part 2: Applications), Goddard Institute for Space Studies, NASA/GSFC.

Halem, M., J. Shukla, Y. Mintz, M. L. Wu, R. Godbole, G. Herman, and Y. Sud, 1979: Comparisons of observed seasonal climate features with a winter and summer numerical simulation produced by the GLAS general circulation model. GARP Pub. Series No. 22, 207-253, WMO, Geneva, Switzerland.

Haltiner, G. J., 1971: Numerical weather prediction. Wiley, 317 pp.

Helfand, H. M., 1979: The effect of cumulus friction on the simulation of the January Hadley circulation by the GLAS model of the general circulation. J. Atmos. Sci., 36, 1827-1843.

Herman, G. F., and W. T. Johnson, 1978: The sensitivity of the general circulation to Arctic sea-ice boundaries: A numerical experiment. Mon. Weather Rev., 106, 1649-1664.

Jaeger, L., 1976: Monatskarten des Niederschlags fur die ganze Erde. Berichte des Deutschen Wetterdienstes, 18, No. 139. Im Selbstverlag des Deutschen Welterdienstes, Offenbach, W. Germany.

Krishnamurthy, V., 1982: The documentation of the Wu-Kaplan radiation parameterization. NASA Tech. Memo. 83926, 93 pp.

Lacis, A. A., and J. E. Hansen, 1974: A parameterization for the absorption of solar radiation in th earth's atmosphere. J. Atmos. Sci., 31, 118-133.

Lin, J. D., J. Alfano, and P. Bock, 1978: Documentation of a ground hydrology parameterization for use in the GISS General Circulation Model. NASA CR158766, 143 pp.

Lorenz, E. N., 1960: Energy and numerical weather prediction. Tellus, 12, 364-373.

Matson, M., 1977: Winter snow cover maps of North America and Eurasia from satellite records, 1966-1976. NOAA Tech. Memo. NESS 84, Washington, DC, 28 pp.

Mintz, Y., and V. Serafini, 1981: Monthly normal global fields of soil moisture and land-surface evapotranspiration. International Symposium on Variations in the Global Water Budget. Oxford, England, August 10-15, 1981. (Manuscript in preparation.)

Moeng, C.-H., and D. A. Randall, 1982: The radiative impact of cumulus cloudiness in a general circulation model. Submitted to the Mon. Wea. Rev.

Oort, A. H., 1964: On estimates of the atmospheric energy cycle. Mon. Wea. Rev., 92, 483-493.

Oort, A. H. and J. P. Peixoto, 1974: The annual cycle of the energetics of the atmosphere on a planetary scale. J. Geophys. Res., 79, 2705-2719.

Phillips, N. A., 1957: A coordinate system having some special advantages for numerical forecasting. J. Meteor., 14, 184-185.

Posey, J. W., and P. F. Clapp, 1964: Global distribution of normal surface albedo. Geofisica International, 4, 33-43.

Randall, D. A., 1982: Performance of the PBL parameterizations in the GLAS and UCLA models. Proceedings of the Workshop on the Planetary Boundary Layer of the European Centre for Medium Range Weather Forecasts, Reading, England 81-118.

Randall, D. A., Y. Sud, J. Shukla, Y. Mintz, V. Serafini, D. H. Kilzmiller, and J. Abeles, 1982a: Gridded monthly boundary conditions for global atmospheric circulation models. NASA Technical Memorandum. (In preparation.)

Randall, D. A., J. A. Abeles, E. J. Pittarelli, and L. Fornito, 1982b: A post-processing package for the GLAS Climate Model. NASA Technical Memorandum. (In preparation.)

Randall, D. A., L. Marx, and J. A. Abeles, 1982c: The GLAS B-grid climate model. NASA Tech. Memo. (In preparation)

Randall, D. A., 1983: Sensitivity of a general circulation model to the parameterization of land-surface evapotranspiration. (In preparation)

Raschke, E., T. H. VonderHaar, M. Pasternak, and W. R. Bandeen, 1973: The radiation balance of the earth-atmosphere system from Nimbus-3 radiation measurements. NASA TND-7249, NASA, Washington, D.C.

Robock, A., 1980: The seasonal cycle of snow cover, sea ice, and surface albedo. Mon. Wea. Rev., 108, 267-285.

Schutz, C., and W. L. Gates, 1971: Global climatic data for surface, 800 mb, 400 mb: January. The Rand Corp., R915-ARPA.

Schutz, C., and W. L. Gates, 1972: Global climatic data for surface, 800 mb, 400 mb: July. The Rand Corp., R-1029-ARPA.

Shapiro, R., 1970: Smoothing, filtering and boundary effects. Rev. Geophys. and Space Phys., 8, 359-387.

Shukla, J., D. Straus, D. A. Randall, Y. Sud, and L. Marx, 1982: Winter and summer simulations with the GLAS Climate Model. NASA Technical Memorandum 83866, 282 pp.

Somerville, R. C. J., P. H. Stone, M. Halem, J. E. Hansen, J. S. Hogan, L. M. Druyan, G. Russell, A. A. Lacia, W. J. Quirk, and J. Tennenbaum, 1974: The GISS model of the global atmosphere. J. Atmos. Sci., 31, 84-117.

Stone, P. H., S. Chow, and W. J. Quirk, 1977: The July climate and a comparison of the January and July climates simulated by the GISS general circulation model. Mon. Wea. Rev., 105, 170-194.

Sud, Y. C., and J. A. Abeles, 1981: Calculation of surface temperature and surface fluxes in the GLAS GCM. NASA Tech. Memo. 82167.

Wu, M. L., 1976: Longwave radiation and its effect on the atmosphere. Ph.D. Thesis, The University of Chicago, 160 pp.

Wu, M. L., L. D. Kaplan, and R. Godbole, 1978: Influence of systematic radiation differences on the dynamics of a model atmosphere. Third Conf. on Atmos. Rad. of the Amer. Meteor. Soc., June 28-30, 1978, Davis, CA.

Wu, M. L., 1980: The exchange of infrared radiative energy in the troposphere. J. Geophys. Res., 85, 4084-4090.